

# 1 Heterotypic Assembly Mechanism Regulates CHIP E3 Ligase Activity

2  
3 Authors: Aniruddha Das<sup>1</sup>, Pankaj Thapa<sup>1</sup>, Ulises Santiago<sup>8</sup>, Nilesh Shanmugam<sup>1</sup>, Katarzyna  
4 Banasiak<sup>1</sup>, Katarzyna Dabrowska<sup>3</sup>, Hendrik Nolte<sup>4,6</sup>, Natalia A. Szulc<sup>1</sup>, Rose M.  
5 Gathungu<sup>5</sup>, Dominik Cysewski<sup>3</sup>, Marcus Krüger<sup>4,7</sup>, Michal Dadlez<sup>3</sup>, Marcin Nowotny<sup>2</sup>, Carlos J.  
6 Camacho<sup>8</sup>, Thorsten Hoppe<sup>4,7</sup>, Wojciech Pokrzywa<sup>1\*</sup>

7  
8 <sup>1</sup>Laboratory of Protein Metabolism, International Institute of Molecular and Cell Biology in  
9 Warsaw, Poland

10 <sup>2</sup>Laboratory of Protein Structure, International Institute of Molecular and Cell Biology in  
11 Warsaw, Poland

12 <sup>3</sup>Institute of Biochemistry and Biophysics, PAS, Warsaw, Poland

13 <sup>4</sup>Institute for Genetics and Cologne Excellence Cluster on Cellular Stress Responses in Aging-  
14 Associated Diseases (CECAD), University of Cologne, Cologne, Germany

15 <sup>5</sup>Metabolomics Core Facility, EMBL, Heidelberg, Germany

16 <sup>6</sup>Current: Max-Planck-Institute for Biology of Ageing, Cologne, Germany

17 <sup>7</sup>Center for Molecular Medicine (CMMC), Faculty of Medicine and University Hospital of  
18 Cologne, 50931 Cologne, Germany

19 <sup>8</sup>Department of Computational and Systems Biology, University of Pittsburgh, Pittsburgh,  
20 Pennsylvania

21 \* Correspondence should be directed to:

22 WP: [wpokrzywa@iimcb.gov.pl](mailto:wpokrzywa@iimcb.gov.pl)

23

## 24 ABSTRACT

25 The E3 ubiquitin ligases CHIP/CHN-1 and UFD-2 team up to accelerate ubiquitin chain formation.  
26 However, it remained largely unclear how the high processivity of this E3 set is achieved. Here we  
27 studied the molecular mechanism and function of the CHN-1/UFD-2 complex in *Caenorhabditis*  
28 *elegans*. Our data show that UFD-2 binding promotes the cooperation between CHN-1 and  
29 ubiquitin-conjugating E2 enzymes by stabilizing the CHN-1 U-box dimer. The HSP-1 chaperone  
30 outcompetes UFD-2 for CHN-1 binding and promotes the auto-inhibited CHN-1 state by acting on  
31 the conserved position of the U-box domain. The interaction with UFD-2 enables CHN-1 to  
32 efficiently ubiquitinate S-Adenosylhomocysteinase (AHCY-1), an enzyme crucial for lipid  
33 metabolism. Our results define the molecular mechanism underlying the synergistic cooperation of  
34 CHN-1 and UFD-2 in substrate ubiquitylation.

35

## 36 KEYWORDS

37

38 *C. elegans*; ubiquitin; proteostasis; E3; CHIP; UFD-2; HSP70; AHCY; lipids

39

40

41

## 42 HIGHLIGHTS

- 43
- 44 • E3 ligase UFD-2 stimulates ubiquitylation activity of CHIP/CHN-1
- 45 • UFD-2 binding promotes dimerization of CHIP/CHN-1 U-box domains and utilization of
- 46 E2 enzymes
- 47 • HSP70/HSP-1 by latching the U-box and TPR domains stabilizes the autoinhibitory state
- 48 of CHIP/CHN-1, limiting interactions with E2s and UFD-2
- 49 • Assembly with UFD-2 enables CHIP/CHN-1 to regulate lipid metabolism by ubiquitylation
- 50 of S-Adenosylhomocysteinase
- 51

## 52 INTRODUCTION

53

54 The ubiquitin-proteasome system (UPS) includes a well-studied enzymatic cascade that transfers

55 the small protein ubiquitin (Ub) onto a protein substrate (Kerscher et al., 2006). The last step in the

56 UPS enzymatic cascade is mediated by ubiquitin-ligases (E3s), the largest and most diverse group

57 of proteins within the UPS responsible for substrate selection and specificity (Komander, 2009;

58 Buetow & Huang, 2016). In some instances, other proteins, i.e., ubiquitin chain elongation factors,

59 or E4s, can be required to achieve efficient polyubiquitylation (poly-Ub) of model substrates. The

60 first described E4 was yeast Ufd2p (Richly et al., 2005), a U-box domain-containing protein that

61 engages Ub via its N-terminal region to assist with Ub chain elongation on pre-ubiquitylated

62 substrates (Koegl et al., 1999; Hatakeyama et al., 2001; Buetow & Huang, 2016).

63

64 CHIP (C-terminus of Hsc70 interacting protein), initially identified as a tetratricopeptide repeat

65 (TPR) protein that interacts with heat shock proteins (Ballinger et al., 1999), is a U-box E3 ubiquitin

66 ligase that mediates ubiquitylation of chaperone client proteins, resulting in their degradation

67 (Murata et al., 2001). Early *Caenorhabditis elegans* studies showed that UFD-2 interacts directly

68 with CHN-1 (the nematode homolog of mammalian CHIP) to form an E3/E4 complex that can

69 efficiently oligo-ubiquitylate the myosin chaperone UNC-45 (Hoppe et al., 2004). By contrast to

70 the model proposed based on these early findings, more recent studies have revealed that UFD-2

71 acts as a true E3 ligase that poly-ubiquitylates UNC-45 independent of CHN-1, suggesting that

72 both UFD-2 and CHN-1 act as E3s in the same or overlapping substrate space (Hellerschmied et

73 al., 2018). A recent study aimed at identifying substrates of human CHIP and the human UFD-2

74 ortholog UBE4B supports the possibility of shared substrate scope (Bhuripanyo et al., 2018).

75 However, despite the vital role of CHN-1/CHIP in protein quality control networks, little is known

76 about its interactions with E3s and the regulation of its activity. To address these questions, we

77 combined *in vitro* and *in vivo* assays with computational approaches and lipidomic and proteomic

78 studies in *C. elegans* and uncovered the mechanism that controls CHN-1 activity. Our results

79 indicate that UFD-2 interacts with the TPR domain of CHN-1 to boost CHN-1 processivity. This

80 binding stabilizes the open conformation of the CHN-1 dimer enabling the U-box dimer to

81 discharge more Ub-conjugating enzymes (E2) in a single ubiquitylation cycle. We also

82 demonstrated that the heat shock protein HSP-1 interacts with the TPR and U-box domain of CHN-  
83 1 to stabilize the closed/auto-inhibitory state of CHN-1 dimer and limits its interaction with E2s  
84 and UFD-2. Furthermore, we identified potential substrates for the CHN-1/UFD-2 pair, including  
85 *S*-adenosylhomocysteinase (AHCY-1), a metabolic enzyme not known to be a client of known heat  
86 shock chaperones. Collectively, our results indicate an interplay between chaperones and UFD-2  
87 in modulating CHIP activity. This processivity switching behavior of CHN-1 has important  
88 implications for its roles in regulating proteostasis, metabolism, and potentially other cellular  
89 processes.

90

## 91 **RESULTS**

92

### 93 **UFD-2 promotes CHN-1 processivity and cooperation with E2s**

94

95 Binding between CHN-1 and UFD-2 was previously demonstrated via yeast two-hybrid and *in*  
96 *vitro* pull-down assays (Hoppe et al., 2004). Beyond the physical interaction, the molecular  
97 regulation of Ub chain elongation by the CHN-1/UFD-2 complex has not been explored in detail.  
98 We performed an *in vitro* analysis of the activity of both E3s individually and in pairs. First, we  
99 chose E2s with which CHN-1 and UFD-2 cooperate in the auto-ubiquitylation (auto-Ub) reaction.  
100 Mammalian CHIPs can functionally interact with various E2s, particularly members of the  
101 UBCH5/UBE2D family (UBCH5a/UBE2D1, -b/2 and -c/3) (Jiang et al., 2001; Soss et al., 2011).  
102 Similarly, CHN-1 cooperates with UBE2D2 to mono-ubiquitylate (mono-Ub) *C. elegans* DAF-2 -  
103 insulin/insulin-like growth factor 1 (IGF-1) receptor *in vitro* (Tawo et al., 2017). To study the  
104 activity of CHN-1 in detail, we compared its ability to self-ubiquitylate in the presence of each of  
105 the UBE2D family proteins separately. We observed that CHN-1 cooperated effectively with  
106 UBE2D1. However, when we performed an auto-Ub reaction with both E3s, we observed a  
107 significant increase in CHN-1 poly-Ub activity, even when the E2 used in the reaction was  
108 UBE2D3, which is not efficiently used by CHN-1 alone (Figure 1A). Furthermore, the presence of  
109 UFD-2 also increases CHN-1 activity with the UBE2N/UBE2V1 E2 complex (Fig. S1B), which  
110 catalyzes the formation of free Ub chains that are then transferred to substrate proteins (Soss et al.,  
111 2011). We also concluded that the induction of E3 ligase activity is unidirectional since we did not  
112 detect any significant changes in the auto-Ub of UFD-2 under the same conditions (Fig. S1A). To  
113 gain insight into CHN-1 processivity, we performed a time-dependent auto-Ub experiment. We  
114 observed no notable changes in the amount of ubiquitylated CHN-1 over time (from 60–180 min);  
115 however, the presence of UFD-2 strongly increased both mono- and poly-Ub of CHN-1 at the  
116 earliest time point (60 min) (Fig. 1B). Using the inactive CHN-1<sup>H218Q</sup> mutant (Tawo et al., 2017),  
117 we observed that auto-Ub CHN-1 is not the result of modification by UFD-2 (Fig. S1C).  
118 Additionally, by deleting the TPR domain of CHN-1( $\Delta$ 110aa), we confirmed its involvement in  
119 UFD-2 binding (Hoppe et al., 2004), as we could not observe modulation of the activity of this  
120 CHN-1 mutant by UFD-2 (Fig. S1D).

121

122 Next, we wanted to verify whether UFD-2 can regulate the poly-Ub processivity of CHN-1  
123 independent of its E3 activity. To examine this mechanism, we used an inactive, recombinant UFD-  
124 2 mutant with a P951A substitution (Ackermann et al., 2016). We found that UFD-2<sup>P951A</sup> inactivity  
125 is due to its inability to bind an E2 enzyme (Fig. S1E). Finally, we performed a CHN-1  
126 ubiquitylation reaction in the presence of UFD-2<sup>P951A</sup>. We detected substantial enhancement in  
127 both the mono- (using lysine-less Ub (Ubk0)) and poly-Ub activity of CHN-1, regardless of the  
128 type of Ub chain (wild-type Ub or variant with substitutions of lysines 29, 48, 63 to arginines  
129 (UbkTR) (Fig. 1C). To rule out the possibility that UFD-2<sup>P951A</sup> retained activity, we also used a  
130 UFD-2 variant (1–910 aa) lacking the entire U-box domain (909–984 aa). We confirmed that this  
131 UFD-2 deletion mutant could stimulate CHN-1 activity, indicating that interaction with some motif  
132 in UFD-2 alone is sufficient to activate CHN-1 (Fig. S1F).

133  
134 Budding yeast Ufd2p can operate as a Ub chain elongation factor by interacting directly with Ub  
135 through its N-terminal region (Liu et al., 2017). Although higher eukaryotes have an ortholog of  
136 yeast Ufd2p, the Ub-interacting motif has little sequence homology (Hänzelmann et al., 2010; Liu  
137 et al., 2017) suggesting that the function of UFD-2 as an E4 is not evolutionarily conserved. To  
138 investigate whether the increased activity of the CHN-1/UFD-2 complex might stem from the  
139 elongation function of UFD-2, we tested whether UFD-2 retained the ability to interact with Ub  
140 using surface plasmon resonance (SPR) experiments. By contrast to Ufd2p, full-length UFD-2 did  
141 not bind linear Ub chains (Fig. 1D). This suggests that during evolution, UFD-2 lost its ability to  
142 elongate Ub chains directly. Unlike yeast Ufd2p, and perhaps to compensate for Ub binding loss,  
143 UFD-2 can induce processivity of its partner CHN-1 (Fig. 1E).

#### 144 145 **UFD-2 induces structural gain of function in CHN-1**

146  
147 To gain mechanistic insight into the role of UFD-2 binding to CHN-1, we performed hydrogen-  
148 deuterium exchange mass spectrometry (HDX-MS) of the dimerization process of both CHN-1  
149 alone and CHN-1 in the presence of UFD-2 (Fig. 2A and S2A). Available crystal structures of  
150 CHIP homologs support our HDX-MS analysis both without a chaperone (Nikolay et al., 2004)  
151 and with HSP90 (Zhang et al., 2005). In the absence of a TPR binding chaperone, only the dimer  
152 domains are revealed by the crystal structure, with no resolution of either the turn in the coil-coil  
153 domain or the TPR domain. Of note, the TPR by itself has only been resolved by NMR, whereas  
154 in the presence of an HSP substrate it stabilizes into its crystal form (Zhang et al., 2005).  
155 Furthermore, mouse CHIP shows that in one of its monomers, bound TPR is further stabilized  
156 against the long helix of its coil-coil domain. We have noted that this interaction is much weaker  
157 in CHN-1 (Thorsten Hoppe - personal communication), suggesting a more dynamic interaction in  
158 worms. Figure 2A and S2A depicts these states, leading to the following interpretation of our HDX-  
159 MS data, which detects at least three dynamical events at 10 s and 60 s. Namely, (a) the turn in the  
160 coil-coil motif (aa 146-152) is stabilized early on upon dimerization of the coil-coil domains; (b)  
161 the TPR domain is stabilized upon recognition by UFD-2, leaving the distal helices aa 21-40 and  
162 92-112 exposed to solvent. At later times the stable TPR stabilizes against the long helix of the

163 coil-coil domain; and, (c) the U-box domain (aa 21-40; 92-112) transitions from a weak interaction  
164 with its coil-coil domain to a stable dimer at longer time scales. As shown in Fig. 2A, we argue  
165 that contrary to CHIP (Ye et al., 2017; Zhang et al., 2005), CHN-1 folds into a symmetric structure  
166 as previously we have indicated that CHN-1 has critical residues that should prevent an asymmetric  
167 fold (Thorsten Hoppe - personal communication). Thus, while it has been shown that HSP90  
168 negatively regulates CHIP activity (Narayan et al., 2015), presumably by blocking the E2 binding  
169 site of one of the protomers (Zhang et al., 2005), our findings of UFD-2 promoting CHN-1  
170 processivity are consistent with a symmetric CHN-1 that upon binding UFD-2 stabilizes the U-box  
171 dimer with two E2 sites available for binding.

172  
173 We conducted a ubiquitylation assay with increasing molar concentrations of UBE2D1 (0.6–6.2  
174  $\mu\text{M}$ ) to confirm this model. We observed that at a constant Ub concentration, increasing E2  
175 concentration led to an increase in CHN-1 activity. However, even at the highest E2 concentration  
176 (6.2  $\mu\text{M}$ ), CHN-1 processivity did not reach the same level as in the presence of inactive UFD-  
177  $2^{\text{P951A}}$  and at an approximately 10-fold lower E2 concentration (0.6  $\mu\text{M}$ ) (Fig. 2B). Thus, the  
178 increased CHN-1 activity in the CHN-1/UFD-2 complex was not due to the increased local E2  
179 concentration but rather to the enhanced processivity of the E2 enzyme bound to the CHN-1 U-  
180 box. To verify this hypothesis, we performed an E2-discharging assay in the presence of CHN-1  
181 alone or after mixing with UFD- $2^{\text{P951A}}$  to track the use of charged-E2 by CHN-1 only. We observed  
182 that in the presence of UFD- $2^{\text{P951A}}$ , CHN-1 could discharge almost twice as much of UBE2D1-Ub  
183 (approximately 6.6  $\mu\text{M}$ ) compared to CHN-1 alone (approximately 3.9  $\mu\text{M}$ ), as indicated by the  
184 accumulation of unused UBE2D1-Ub (Fig. 2C). Next, we performed another E2-discharging assay  
185 over time (0–30 min) to verify whether the increased utilization of charged E2 by the CHN-1/UFD-  
186  $2^{\text{P951A}}$  pair was due to altered E2-E3 ubiquitin transfer dynamics. We noted that within the initial 5  
187 minutes, the system achieved the maximum usage of charged E2, and no significant change in the  
188 level of available UBE2D1-Ub was observed over time (Fig S2B). Summarizing, our data indicate  
189 that UFD-2 acts as a preconditioner for the conformational flexibility of CHN-1, promoting  
190 dimerization of the U-box domains and thereby enabling their full functionality.

### 191 192 **HSP-1 and UFD-2 modulate CHN-1 processivity by stabilizing its inactive and active** 193 **conformations, respectively**

194  
195 The three TPR domains in CHIP act as a binding platform for C-terminal peptides in the Hsp70  
196 and Hsp90 chaperones, containing a conserved EEVD motif (Zhang et al., 2005; Paul & Ghosh,  
197 2014; Zhang et al., 2015). Since CHN-1 also binds UFD-2 via the TPR domain, we investigated  
198 whether HSP-1 (the nematode Hsp70 orthologue) or DAF-21 (the nematode Hsp90 orthologue)  
199 could interfere with the activity of the CHN-1/UFD-2 complex. We first examined protein-protein  
200 interactions between CHN-1 and UFD-2, HSP-1, or DAF-21 using enzyme-linked immunosorbent  
201 assays (ELISAs). CHN-1 showed a higher affinity for HSP-1 and DAF-21 compared to UFD-2  
202 (Fig. S3A). To verify the influence of HSP-1 and DAF-21 on the activity of the CHN-1/UFD-2  
203 pair, we performed auto-Ub reactions in the presence of the chaperones. HSP-1 significantly

204 reduced the auto-Ub activity of CHN-1 and blocked the stimulatory capacity of UFD-2 in this  
205 process (Fig. 3A). Negative regulation of CHIP auto-Ub by HSP70 has been previously reported,  
206 but the molecular basis is unclear (Narayan et al., 2015). Removal of the C-terminal EEVD motif  
207 deprived HSP-1 of its inhibitory effect. By contrast, DAF-21 did not affect the UFD-2-enhanced  
208 activity of CHN-1 (Fig. 3A).

209  
210 Next, we performed peptide mapping on peptide microarrays to pinpoint the interaction interface  
211 between the two ligases. For this, we used purified CHN-1 tagged with His::SUMO and  
212 His::SUMO alone (as control). These proteins were incubated on two UFD-2 peptide microarrays  
213 consisting of peptides of lengths 7 and 13 aa. This was followed by staining with secondary and  
214 control antibodies and reading using the LI-COR Odyssey Imaging System. Signal enrichment  
215 analysis suggested that the two consensus sequences EAKAELEEE and EEYDDVPE, were the  
216 predominant interactor motif. HSP70/90 uses a similar acidic C-terminal peptide with an EEVD  
217 sequence to bind to the TPR domain of target proteins (Scheufler et al., 2000; Gazda et al., 2013),  
218 and HSP-1 C-terminal EEVD peptide affected CHN-1 activity (Fig. 3B). Therefore, we examined  
219 whether the identified UFD-2 peptides could also regulate CHN-1. To this end, we performed  
220 CHN-1 auto-Ub reactions in the presence of the UFD-2-derived peptides identified in the peptide  
221 microarray data. We found that only the KKEYEAKAELEEEYDDVP peptide from UFD-2  
222 significantly stimulated CHN-1 auto-Ub (Fig. 3C). An EEYD sequence is present in this peptide,  
223 suggesting that UFD-2 can utilize an EEVD-like motif for CHN-1 binding. Furthermore, multiple  
224 sequence alignment analysis revealed that in the EEYD motif of UFD-2, the amino acid Tyr (Y) is  
225 evolutionarily conserved among higher eukaryotes (Fig. S3B). To further define the functional role  
226 of the EEYD motif from UFD-2, we generated a chimeric recombinant HSP-1 protein carrying N-  
227 terminal EEYD instead of EEVD. Strikingly, we observed stimulation of CHN-1 auto-Ub when  
228 EEYD was introduced into HSP-1 – an opposite effect compared with that of wild-type HSP-1,  
229 which inhibited the reaction (Fig. S3C). Chimeric HSP-1<sup>EEYD</sup> also exerted a slightly stimulatory  
230 effect on UBE2D1-Ub discharging by CHN-1 (Fig. S3D). This suggests that the CHN-1 activity  
231 switch can be regulated by its binding partners' EEV(Y)D motifs.

232  
233 To assess the contribution of the particular regions of the CHN-1 TPR domain, we generated its  
234 truncation variants. We showed that the first 87 amino acids (aa) ( $\Delta 87$ ) are not responsible for the  
235 interaction with UFD-2 and HSP-1, and therefore are not involved in the modulation of CHN-1  
236 processivity. In contrast, removing the subsequent eight residues ( $\Delta 95$  variant) abrogated the CHN-  
237 1 poly-ubiquitylation activity. Interestingly, the stimulating effect of UFD-2 was still observed,  
238 as evidenced by an increase in monoubiquitylated CHN-1 <sup>$\Delta 95$</sup>  (Fig. S3E). CHN-1 <sup>$\Delta 95$</sup>  has residues  
239 that may be involved in the interaction with UFD-2, including D110 and subsequent twists and  
240 helices (Fig. S3F). Indeed, the CHN-1 <sup>$\Delta 110$</sup>  mutant, which lacks D110, does not show any gain of  
241 activity in the presence of UFD-2 (Fig. S1D). It is known that a position homologous to D110 in  
242 mouse CHIP (D135) is involved in the binding of HSP's, which suggests that this residue is also  
243 important for the interaction with UFD-2 EEYD peptide (Fig. S3F).

244

245 To understand why HSP-1 and UFD-2 peptides exhibit distinct effects on CHN-1 activity, we  
246 looked closely at the mechanism by which increased HSP90 and HSP70 concentration reduces  
247 CHIP activity (Narayan et al., 2015). As noted, HSP90 stabilizes an autoinhibit monomer in mouse  
248 CHIP (Zhang et al., 2005). Strikingly, this state entails a salt-bridge bridge between HSP90 D501  
249 and CHIP R273, latching the U-box and TPR domains (Fig. S3G). This observation suggests that  
250 chaperone binding can directly restrain U-box from participating in Ub processivity. To show that  
251 a similar mechanism is at play in inhibiting ubiquitylation by HSP-1, we mutated R230  
252 (homologous position to R273 in CHIP) to alanine to weaken the CHN-1 U-box interaction with  
253 the HSP-1 peptide and thus abrogate its inhibitory effect. Indeed, we observed significantly reduced  
254 inhibition of CHN-1R230A/UFD-2 complex by HSP-1 (Fig. 3D). Moreover, the addition of HSP-  
255 1 blocked the utilization of charged E2 by the CHN-1/UFD-2P951A complex (Fig. 3E). This agrees  
256 with the model indicating that by interacting with the TPR and U-box domain, HSP-1 stabilizes  
257 the autoinhibited state of CHN-1, affecting interaction with E2 enzymes (Fig. 3F). On the other  
258 hand, UFD-2 can avoid interacting with R230 by, for example, forming a helix that cannot extend  
259 toward the U-box, and induces uncorrelated mobility of the TPR domains with respect to the U-  
260 box domains, promoting the steady-state open conformation of CHN-1 (Fig. 3F).

261

## 262 **The CHN-1/UFD-2 pair regulates phosphatidylcholine synthesis via AHCY-1**

263

264 We next wished to establish the functional consequences of CHN-1/UFD-2 cooperation *in vivo*.  
265 Based on our *in vitro* studies, we hypothesized that *in vivo* CHN-1, when functioning alone, would  
266 display insufficient poly-Ub activity and mainly mono-Ub substrates. Indeed, Tawo and colleagues  
267 showed that CHN-1/CHIP mono-Ub the DAF-2 insulin receptor (Tawo et al., 2017). We further  
268 assumed that the interaction with UFD-2 would trigger the poly-Ub activity of CHN-1,  
269 consequently leading to efficient degradation of its specific substrates. Thus, to understand the role  
270 of CHN-1 and UFD-2 *in vivo*, we decided to identify such substrates. We searched for proteins  
271 whose levels increase after deletion of CHN-1 (substrate ubiquitylation by CHN-1 would be  
272 affected directly) or UFD-2 (CHN-1 would not be stimulated to efficiently poly-Ub its substrates).  
273 To define the consequences of *chn-1* and *ufd-2* deletion on the *C. elegans* proteome and to detect  
274 proteins that accumulate in the deletion mutants in an unbiased way, we performed label-free mass  
275 spectrometry (LC-MS/MS)-based proteomics experiment. We analyzed *chn-1(by155)*, *ufd-*  
276 *2(tm1380)*, and *chn-1(by155); ufd-2(tm1380)* double-mutant worms by single-shot LC-MS/MS  
277 gradients in 5 biological replicates. To obtain a view of the global structure of the data, we  
278 performed dimensional reduction using principal component analysis (PCA). We noticed that the  
279 proteomes of *chn-1(by155)* and *chn-1(by155); ufd-2(tm1380)* mutants clustered closer together  
280 than did those of *chn-1(by155)* and *ufd-2(tm1380)* (Fig. S4A). We hypothesized that potential  
281 substrates should accumulate in all mutants; therefore, we filtered the set of significantly altered  
282 proteins requiring a two-fold enrichment in all mutants versus the N2 control strain. We obtained  
283 65 potential substrate candidates and visualized them via hierarchical clustering (Fig. S4B, C and  
284 Supp. Table 1). These potential substrates were enriched in metabolic processes, including lipid  
285 biosynthesis, as shown via Gene Ontology over-representation analysis (Fig. S4D), and among

286 them, we identified the AHCY-1 enzyme (Fig. 4A and S4C). AHCY-1 catalyzes the reversible  
287 hydrolysis of *S*-adenosylhomocysteine (SAH) to homocysteine and adenosine (Palmer and Abeles,  
288 1976; 1979) (Fig. 4B). Despite the fundamental role of AHCY-1 in metabolism, its regulatory  
289 mechanisms are still enigmatic. In a yeast two-hybrid screen using a *C. elegans* cDNA library, we  
290 identified AHCY-1 as the prominent interactor of CHN-1 (Fig. S4E). We confirmed the interaction  
291 between the two proteins in worms via co-immunoprecipitation (Fig. S4F). Next, we tested whether  
292 AHCY-1 is a CHN-1 substrate by performing *in vitro* ubiquitylation assays with recombinantly  
293 expressed proteins. We confirmed that recombinant AHCY-1 is a specific substrate of CHN-1 that  
294 UFD-2 does not ubiquitylate (Fig S4H). Furthermore, in the presence of UFD-2, CHN-1 poly-Ub  
295 AHCY-1 more effectively, and the level of this modification was reduced by HSP-1 (Fig. 4C, S4G).  
296 The cooperation between CHN-1 and UFD-2 is also consistent with the detection of a similar  
297 increase in the AHCY-1 level in *chn-1(by155)*, *ufd-2(tm1380)*, and double mutant worms in our  
298 proteomic analysis (Fig. 4A). To further validate this observation, we monitored the endogenous  
299 level of AHCY-1 via western blotting of total lysates of wild-type worms, *chn-1(by155)* and *ufd-*  
300 *2(tm1380)* mutant worms, and worms overexpressing *chn-1* treated with the proteasome (MG132)  
301 and DUB (*N*-methylmaleimide, NEM) inhibitors. We did not observe any significant changes in  
302 the AHCY-1 level, which, according to our other observations, is a stable and abundant protein in  
303 *C. elegans*. However, immunoblotting analysis with anti-AHCY-1 antibodies detected higher  
304 molecular weight smeared bands, likely corresponding to polyubiquitinated AHCY-1 species.  
305 These AHCY-1 modifications were more abundant when *chn-1* was over-expressed and were  
306 reduced in *chn-1(by155)* and *ufd-2(tm1380)* mutant worms compared with the AHCY-1 status in  
307 wild-type animals (Fig. 4D). These data suggest that CHN-1 regulates AHCY-1 *via* an E3 activity  
308 triggered by UFD-2.

309  
310 Elevated homocysteine levels are linked to the deregulation of lipid metabolism and increased fat  
311 accumulation, apparent after RNA interference (RNAi) depletion of AHCY-1 in worms (Vrablik  
312 et al., 2015; Visram et al., 2018). Using the lipophilic fluorophore RediStain WormDye Lipid  
313 Green to stain and quantify the fat content of *C. elegans*, we confirmed that AHCY-1 depletion  
314 increases the abundance of lipids in wild-type worms by almost 60%. Overexpression of *chn-1*  
315 caused an increase in total lipid content to the similar level detected in *ahcy-1* RNAi-treated worms,  
316 and this effect was not further enhanced by AHCY-1 depletion (Fig. 4E). Interestingly, mutations  
317 in *chn-1* and *ufd-2* cause a reduction in overall lipid levels and uncouple the stimulation of lipid  
318 biogenesis induced by *ahcy-1* RNAi (Fig. 4E). Synthesis of phosphatidylcholine (PC) from  
319 phosphatidylethanolamine (PE) via the *de novo* phospholipid methylation pathway requires a  
320 significant amount of SAM and is particularly sensitive to SAH levels (Tehlivets, 2011). Consistent  
321 with our assumption that deletion of either *chn-1* or *ufd-2* would positively affect AHCY-1  
322 stability, leading to intensification of SAM-dependent methylation and PE to PC conversion, we  
323 noted that the ratio of PC to PE increased in *chn-1(by155)* and *ufd-2(tm1380)* worms (Fig. 4F). In  
324 conclusion, our data suggest a functional role for the CHN-1/UFD-2 complex in AHCY-1-  
325 dependent lipid metabolism regulation.

326



## 327 DISCUSSION

328  
329 The different conformations achieved by dynamic and flexible motifs are important for the  
330 functionality of various E3 ligases (Faull et al., 2019; Kamadurai et al., 2013; Liu and Nussinov,  
331 2011; Narayan et al., 2015). The crystal structure of murine CHIP E3 bound to an HSP-90  
332 decapeptide containing an EEVD motif revealed an asymmetric dimerization in which the two  
333 CHIP protomers adopt different conformations. In this “closed” state, only one of the U-box  
334 domains in the dimer is accessible for E2 binding, and the other is blocked by the TPR domain  
335 (Zhang et al., 2005). In agreement with a computational model of human CHIP (Ye et al., 2017),  
336 our homology modeling of the CHN-1 dimer suggested that it can take the form of both a  
337 metastable symmetric dimer in which both U-box domains can simultaneously bind E2 ubiquitin-  
338 conjugating enzymes and asymmetric dimer with low ubiquitylation activity. We showed that the  
339 interaction of E3 UFD-2 with the CHN-1 TPR domain reduces its dynamics and thus its blocking  
340 of U-box domains. In this steady-state open conformation, CHN-1 achieved high poly-Ub activity  
341 due to the full functionality of the U-box dimer. Consistently, in the E2 discharging assay, we  
342 observed a two-fold increase in the utilization of charged E2 by the CHN-1/UFD-2<sup>P951A</sup> complex  
343 compared with that of CHN-1 alone. Here, UFD-2 acts as a pre-conditioning factor to influence  
344 the conformational flexibility of CHN-1, allowing higher processivity at the initial phase; therefore,  
345 we did not observe any further change in our E2 discharging reaction kinetics with increasing time.  
346 Using various ubiquitin variants, we showed that not only poly-Ub but also CHN-1 mono-Ub,  
347 which is the rate-limiting step of ubiquitylation, is also enhanced upon UFD-2 binding. We also  
348 found that UFD-2 activity is unaffected in the complex and that the two ligases are not substrates  
349 for each other.

350  
351 The N-terminal TPR domain of CHIP has been shown to interact specifically with the C-terminal  
352 EEVD motif of HSP70 and HSP90 (Zhang et al., 2005; Xu et al., 2006; Graf et al., 2010). We  
353 discovered that UFD-2 uses a slightly modified motif - EEYD to engage the CHN-1 TPR domain.  
354 Furthermore, we demonstrated that only the presence of a UFD-2 peptide containing the EEYD  
355 sequence was sufficient to promote CHN-1 activity. In contrast, the *C. elegans* HSP70 homolog,  
356 HSP-1, negatively regulates CHN-1 and CHN-1/UFD-2 complex activity by promoting its auto-  
357 inhibited (closed) CHN-1 state. GHFDPVTR sequence in the U-box domain is evolutionarily  
358 conserved in CHIP from different species, but its role was not previously known. Here we showed  
359 that CHN-1 activity is negatively regulated by the interaction between positions associated with  
360 the EEVD motif of HSP-1 and the conserved R230 position in the GHFDPVTR sequence. Through  
361 direct interactions with the TPR and U-box domain of CHN-1, HSP-1 brings both regions to  
362 proximity impairing the U-box dimer. This depends only on the local interaction of the C-terminus  
363 of HSP-1 with the U-box, not on the steric hindrance of E2 access to U-box domains by the whole  
364 chaperone. In co-crystal with CHIP, HSP90 also forms hydrogen bonds (H-bonds) between T and  
365 S in its C-terminal peptide (TSRMEEVD) and TPR of CHIP (Zhang et al., 2005). The existence of  
366 these H-bonds between the HSP-1 peptide (GPTIEEVD) and CHN-1 is not apparent. However, the  
367 C-terminal sequence of HSP-1 is rich in glycines that may tailor the binding more efficiently by

368 forming H-bonds with the CHN-1 backbone, possibly leading to a very close interaction.  
369 Accordingly, the C-terminal HSP70 peptide blocks CHIP activity markedly greater than the HSP90  
370 peptide, which binds to the CHIP TPR domain weaker than the HSP70 peptide (Narayan et al.,  
371 2015). We also observed that worm DAF-21/HSP90 has a lower affinity for CHN-1 and does not  
372 affect CHN-1 activity, unlike HSP-1. Thus, the mechanism in which the degree of interaction  
373 depends on the C-terminal sequence of the chaperones is conserved and correlates with the  
374 stabilization of the autoinhibited CHN-1/CHIP dimer. Presumably, high CHN-1 processivity is  
375 undesirable for HSPs as it could lead to an imbalance between chaperone-mediated  
376 folding/maturation and degradation, inducing the latter. We cannot exclude the influence of  
377 posttranslational factors or the cellular environment on the level of regulation of CHN-1 activity  
378 by HSP-1 and UFD-2.

379  
380 Previous research has established that CHIP participates in protein quality control by routing a  
381 wide range of chaperone substrates for degradation (Joshi et al., 2016). Our observations suggest  
382 an alternative, non-quality control role for the CHN-1/UFD-2 complex. We identified AHCY-1 as  
383 a novel substrate of the CHN-1/UFD-2 complex. AHCY-1 is the only eukaryotic enzyme capable  
384 of hydrolyzing SAH, which is essential for SAM-dependent methylation (Cantoni, 1975). Recent  
385 findings support the importance of CHIP in regulating the methylation status of the cellular  
386 proteome by mediating proteasomal turnover of the SAM-dependent methyltransferases PRMT1,  
387 PRMT5, and EZH2 (Zhang et al., 2016; Bhuripanyo et al., 2018). However, further studies are  
388 necessary to delineate the involvement of the CHN-1/UFD-2 complex in modulating the cellular  
389 methylation potential. In summary, our data provide mechanistic insights into the distinct  
390 regulation of CHN-1/CHIP activity by HSP70 and UFD-2 and the processivity of non-chaperone  
391 CHIP substrates.

392

### 393 **LIMITATIONS OF THE STUDY**

394  
395 Our study elucidates the possible mechanism of action of CHN-1 in the presence of various partner  
396 proteins based on the biochemical data and the available structure of CHIP. However, we were  
397 unable to provide detailed insights into the structure of CHN-1 in association with UFD-2 or HSPs  
398 as we were unable to obtain a co-crystal after various attempts. Furthermore, we could not isolate  
399 the essential amino acids of CHN-1 that are required for interaction with UFD-2 and HSP-1.  
400 Therefore, we cannot exclude the possibility that multiple CHN-1 motifs may be involved in the  
401 interactions. In addition to presenting a novel, non-quality-controlling role for the CHN-1/UFD-2  
402 pair, we cannot comment on the physiological factors that regulate this E3 complex assembly.

403

### 404 **LEGENDS**

405

406 **Figure 1: UFD-2 activates CHN-1.** A) Auto-Ub of recombinant CHN-1 and UFD-2 was carried  
407 out using the E2s UBE2D1, UBE2D2, and UBE2D3. CHN-1 ubiquitylation was assessed via

408 western blotting using CHN-1-specific antibodies. B) Time-dependent (60, 90, 180 min) auto-Ub  
409 of CHN-1 was performed as indicated using wild-type ubiquitin (Ub<sup>WT</sup>) or a lysine-free variant  
410 (Ub<sup>NoK</sup>). Protein samples were resolved via SDS-PAGE and immunoblotted with anti-CHN-1  
411 antibodies. C) Auto-Ub was performed as indicated using recombinant CHN-1 and UFD-2<sup>P951A</sup>,  
412 UBE2D1 E2, Ub<sup>WT</sup>, Ub<sup>NoK</sup> or Ub with substitutions of lysines 29, 48, 63 to arginines (Ub<sup>3KTR</sup>).  
413 Protein samples were resolved via SDS-PAGE and immunoblotted with anti-CHN-1 antibodies.  
414 D) Surface plasmon resonance (SPR) sensorgrams of the interaction between linear di-Ub (M1-  
415 linear from UbiQ) and *C. elegans* UFD-2 (red) or *S. cerevisiae* Ufd2p (blue). Y-axis: response unit  
416 (RU) value. X-axis: molar concentration of linear di-Ub. E) *In vitro* auto-ubiquitylation of CHN-1  
417 in the presence of recombinant *C. elegans* UFD-2 and *S. cerevisiae* Ufd-2p, and UBE2D1 E2.  
418 Protein samples were resolved via SDS-PAGE and immunoblotted with anti-CHN-1 antibodies.  
419 Immunoblots representative of n = 3 experiments are shown.

420  
421 **Figure 2: UFD-2 stabilizes CHN-1 U-box dimer.** A) HDX-MS was used to analyze changes in  
422 the structural dynamics of residues within CHN-1 when in complex with UFD-2. The diagram  
423 model represents regions of retarded (red) and enhanced (blue) exchange in CHN-1 (upper panel).  
424 Schematics showing the domain organization of CHN-1 and the rate of deuterium exchange  
425 (colored box: blue, light red, medium red, dark red) in the different domains upon interaction with  
426 UFD-2 (lower panel). B) Auto-Ub of CHN-1 was performed as indicated using increasing amounts  
427 (0.6, 1.2, 2.5, 6.2 μM) of UBE2D1 or 0.6 μM UBE2D1 after complexing CHN-1 with 0.2 μM of  
428 recombinant UFD-2<sup>P951A</sup>. Protein samples were resolved via SDS-PAGE and immunoblotted with  
429 anti-CHN-1 antibodies. Quantification of the change in unmodified CHN-1 levels. Y-axis against  
430 the intensity of the unmodified band in each lane. Analysis performed using GraphPad Prism. C)  
431 E2 discharging assay of Ub-charged UBE2D1 in the presence of CHN-1/UFD-2<sup>P951A</sup>. The reaction  
432 was stopped after the indicated time via heat inactivation in native conditions. Protein samples  
433 were resolved via SDS-PAGE and immunoblotted with anti-Ub antibodies. (left panel).  
434 Quantification of available charged UBE2D1. Y-axis against the intensity of the UBE2D1-Ub  
435 signal from each and X-axis plotted against the μM concentration of UBE2D1-Ub (right panel).  
436 Immunoblots representative of n = 3 experiments are shown.

437  
438 **Figure 3: UFD-2 stabilizes an open/active, and HSP-1 stabilizes a closed/non-active CHN-1**  
439 **conformation.** A) *In vitro* auto-Ub was performed as indicated using recombinant CHN-1  
440 complexed with UFD-2 in the presence of recombinant DAF-21, DAF-21ΔEEVD, HSP-1, or HSP-  
441 1ΔEEVD. Protein samples were resolved via SDS-PAGE and immunoblotted with anti-CHN-1  
442 antibodies. B) On top schematics of the HSP-1 peptide sequence used in ubiquitylation reaction.  
443 Auto-Ub was performed as indicated using recombinant CHN-1 and HSP-1 derived peptide.  
444 Protein samples were resolved via SDS-PAGE and immunoblotted with anti-CHN-1 antibodies.  
445 Below, quantification of the changes (%) in (un)modified CHN-1 levels. Immunoblots  
446 representative of n = 3 experiments are shown. C) Schematics of the UFD-2 peptide sequences  
447 used in further ubiquitylation reactions (left panel). Auto-Ub was performed as indicated using  
448 recombinant CHN-1 and UFD-2 derived peptides. Protein samples were resolved via SDS-PAGE

449 and immunoblotted with anti-CHN-1 antibodies (middle panel). Quantification of the changes (%)  
450 in (un)modified CHN-1 levels (right panel). D) Auto-Ub was performed as indicated using  
451 recombinant CHN-1<sup>R230A</sup>, UFD-2 and HSP-1. Protein samples were resolved via SDS-PAGE and  
452 immunoblotted with anti-CHN-1 antibodies. Immunoblots representative of n = 3 experiments are  
453 shown. E) E2 discharging assay of Ub-charged UBE2D1 in the presence of a ternary mixture of  
454 recombinant CHN-1/UFD-2<sup>P951A</sup>/HSP-1. The reaction was stopped after the indicated time via heat  
455 inactivation in native conditions. Protein samples were resolved via SDS-PAGE and  
456 immunoblotted with anti-Ub antibodies. F) Model of the UFD-2 activation and HSP-1 inhibition  
457 of CHN-1. Dimeric CHN-1 with TPR, U-box, and helix-turn-helix (HH) indicated by magenta,  
458 gold and cyan color, respectively. UFD-2 and HSP-1 peptides in yellow with indicated amino acid  
459 positions in the full-length proteins.

460  
461 **Figure 4: The CHN-1/UFD-2 pair regulates lipid metabolism via AHCY-1.** A) Endogenous  
462 levels of AHCY-1 in N2 (wild-type), *chn-1(by155)*, *ufd-2(tm1380)*, and *chn-1(by155); ufd-*  
463 *2(tm1380)* mutant worms reported as Z-scores from LC-MS/MS analysis. B) Schematic diagram  
464 representing the core function of AHCY. AHCY catalyzes the reversible hydrolysis of SAH (S-  
465 adenosylhomocysteine) to Hcy (Homocysteine). Accumulation of SAH inhibits PC  
466 (Phosphatidylcholines) synthesis from PE (Phosphatidylethanolamines). C) Ubiquitylation of  
467 recombinant AHCY-1 was performed as indicated using recombinant CHN-1 and UFD-2,  
468 UBE2D1 E2, Ub<sup>WT</sup>, or Ub<sup>K48</sup> and Ub<sup>K63</sup> only Ub variants. Protein samples were resolved via SDS-  
469 PAGE and immunoblotted with anti-AHCY-1 antibodies. Bands labeled as unmodified AHCY-1,  
470 mono-Ub AHCY-1, di-Ub AHCY-1, poly-Ub AHCY-1 (left panel). Quantification of the changes  
471 (%) in (un)modified AHCY-1 levels (right panel). D) Endogenous levels of AHCY-1 in N2 (wild-  
472 type), *chn-1(by155)*, CHN-1::FLAG (OE), and *ufd-2(tm1380)* young adult worms treated with a  
473 proteasome inhibitor (MG132, 10 $\mu$ M) or DUB inhibitor (NEM, 100mM). Protein samples were  
474 resolved via SDS-PAGE and immunoblotted with anti-AHCY-1 antibodies. Tubulin served as a  
475 loading control. Immunoblots representative of n = 3 experiments are shown. E) Total lipid content  
476 in N2 (wild-type), *chn-1(by155)*, *ufd-2(tm1380)*, *chn-1(by155); ufd-2(tm1380)*, and CHN-1::FLAG  
477 (OE) young adult worms grown on control and *ahcy-1* RNAi feeding plates. Data are means  $\pm$   
478 SEM, p  $\leq$  0.001 (\*\*\*). Higher fluorescence intensity indicates increased lipid levels. F) Ratio of  
479 phosphatidylcholine (PC) to phosphatidylethanolamine (PE) in N2 (wild-type), *chn-1(by155)*, and  
480 *ufd-2(tm1380)* young adult worms.

481  
482 **Supplementary Figure S1:** A) Auto-Ub of UFD-2 was performed as indicated using E2s  
483 UBE2N/Uev1a, UBE2D1, or UBE2D3, and Ub<sup>WT</sup> or Ub<sup>NoK</sup>. Protein samples were resolved via  
484 SDS-PAGE and immunoblotted with anti-UFD-2 antibodies. B) Auto-Ub was performed as  
485 indicated using UBE2N/Uev1a and UBE2D1 E2s. Protein samples were resolved via SDS-PAGE  
486 and immunoblotted with anti-Ub antibodies. C) Ubiquitylation of recombinant CHN-1<sup>H218Q</sup> mutant  
487 was performed as indicated. Protein samples were resolved via SDS-PAGE and immunoblotted  
488 with anti-CHN-1 antibodies. D) Auto-Ub of recombinant CHN-1 <sup>$\Delta$ 110</sup> was performed as indicated  
489 using UBE2D1 E2. Protein samples were resolved via SDS-PAGE and immunoblotted with anti-

490 CHN-1 antibodies. E) Co-immunoprecipitation of ubiquitin-charged GST-UBE2D1 from a  
491 mixture of recombinant GST-UBE2D1 and CHN-1, GST-UBE2D1 and UFD-2<sup>P951A</sup>, and the  
492 ternary mixture of GST-UBE2D1, CHN-1 and UFD-2<sup>P951A</sup> using Dynabeads conjugated with anti-  
493 GST antibody. Protein samples were resolved via SDS-PAGE and immunoblotted with anti-GST,  
494 anti-UFD-2, and anti-CHN-1 antibodies. F) Auto-Ub was performed as indicated using  
495 recombinant UFD-2, UFD-2<sup>P951A</sup>, or UFD-2<sup>ΔUbox</sup>. Bands labeled as unmodified CHN-1, mono-Ub  
496 CHN-1, and poly-Ub CHN-1. Below, quantification of the changes (%) in (un)modified CHN-1  
497 levels. Immunoblots representative of n = 3 experiments are shown.

498  
499 **Supplementary Figure S2:** A) Differential Woods plots present the difference in fractional  
500 deuterium uptake between two biological states - CHN-1 and CHN-1 in the presence of wild-type  
501 UFD-2. The X-axis represents the position in sequence for a peptide (the x value indicates the  
502 peptide length). The Y-axis presents the difference in fractional deuterium uptake with the Y-error  
503 bar indicating the uncertainty of the measurement from three independent replicates of the  
504 experiment. Positive values indicate stabilization of the region upon complex formation. Dotted  
505 lines indicate the confidence limit at 95% calculated using the Houde test (Houde et al., 2011). The  
506 upper and lower panels show results after 10 and 60 seconds of H/D exchange, respectively. B) E2  
507 discharging assay of Ub-charged UBE2D1 by the recombinant CHN-1/UFD-2<sup>P951A</sup>. The reaction  
508 was stopped after the indicated time via heat inactivation in native conditions. Protein samples  
509 were resolved via SDS-PAGE and immunoblotted with anti-Ub antibodies.

510  
511 **Supplementary Figure S3:** A) Titration ELISA assay to determine the dissociation constant ( $K_D$ )  
512 between DAF-21, HSP-1, UFD-2, and CHN-1. Y-axis: CHN-1 concentration ( $\mu\text{M}$ ). X-axis:  
513 absorbance (OD) at 450 nm. Below, a table showing the  $K_D$  value (nM) of the corresponding protein  
514 with recombinant CHN-1. B) Multiple sequence alignment (MSA) of UFD-2 orthologs from  
515 different species. Orthologous sequences (from Orthologous Group ID ENOG5038DSP) of  
516 selected species were obtained from the eggNOG5 database (Huerta-Cepas et al., 2019) and aligned  
517 using the T-Coffee web server with default parameters (Di Tommaso et al., 2011; Notredame et  
518 al., 2000). Vertebrates possess two UFD-2 orthologs, which have been independently annotated.  
519 MSA was visualized in Jalview Desktop software (Waterhouse et al., 2009) with residues colored  
520 according to their physicochemical properties; conserved tyrosine (Y) residues and the EEYD  
521 motif in *C. elegans* are highlighted in white frames. C) Auto-Ub was performed as indicated using  
522 recombinant CHN-1 complexed with HSP-1 and HSP-1<sup>EEYD</sup>. Protein samples were resolved via  
523 SDS-PAGE and immunoblotted with anti-CHN-1 antibodies. Immunoblots representative of n = 3  
524 experiments are shown. D) E2 discharging assay of Ub-charged UBE2D1 in the presence of CHN-  
525 1 or CHN-1/HSP-1<sup>EEYD</sup>. The reaction was stopped after the indicated time via heat inactivation in  
526 native conditions. Protein samples were resolved via SDS-PAGE and immunoblotted with anti-Ub  
527 antibodies. Immunoblots representative of n = 3 experiments are shown. E) *In vitro*  
528 autoubiquitylation was performed as indicated using recombinant CHN-1<sup>Δ87</sup> or CHN-1<sup>Δ95</sup>  
529 truncation mutants in the presence of UFD-2, DAF-21, DAF-21ΔEEVD, HSP-1, and HSP-  
530 1ΔEEVD. Samples were analyzed by SDS-PAGE and immunoblotted with anti-CHN-1 antibodies.

531 Immunoblots representative of  $n = 3$  experiments are shown. F) Model of the CHN-1 TPR domain  
532 docked with UFD-2 EEYD peptide with 1-86 residues of CHN-1 colored in orange and 87-95  
533 residues in magenta colors that sequester the EEYD motif away from R230 residue of CHN-1. G)  
534 Co-crystal structure of the mice CHIP TPR domain showing interaction with HSP90 EEVD peptide  
535 (2C2L) shows R273 (conserved in CHN-1 as R230) in proximity close enough to interact with  
536 D501 of HSP90.

537  
538 **Supplementary Figure S4:** A) PCA analysis showing the first and second principal components  
539 of the significantly altered proteins (ANOVA FDR < 0.05) performed in the Perseus software. The  
540 percentage of explained variance is provided on the axis labels as a percentage. B) Schematic  
541 representation of the number of identified proteins in a single-shot analysis of LC-MS/MS  
542 gradients in 5 biological replicates that led to the identification of proteins with a significant change  
543 in abundance in *chn-1(by155)*, *ufd-2(tm1380)*, and *chn-1(by155); ufd-2(tm1380)* worms (two-fold  
544 enrichment in all mutants versus N2 (wild-type) animals). C) Hierarchical clustering of the Z-Score  
545 of proteins whose levels increased in *chn-1(by155)*, *ufd-2(tm1380)*, and *chn-1(by155); ufd-*  
546 *2(tm1380)* mutant worms (two-fold enrichment in all mutants versus N2 (wild-type) animals from  
547 LC-MS/MS experiment). D) Gene Ontology biological process terms found to be associated with  
548 *C. elegans* genes upregulated (minimum two-fold enrichment versus N2 (control), with FDR <  
549 0.05 for ANOVA or pairwise t-test) in all mutants; all proteins detected in LC-MS/MS analysis  
550 constituted a reference set. Over-representation analysis was performed using the WebGestalt web  
551 server with default parameters (Liao et al., 2019). FDR was controlled to 0.25 using the Benjamini-  
552 Hochberg method for multiple testing. E) Yeast 2-hybrid prey fragment analysis. Schematic  
553 representations of the AHCY-1 fragments interacting with CHN-1. The coding sequence for CHN-  
554 1 was used as bait to screen a random-primed *C. elegans* mixed-stage cDNA library. The selected  
555 interaction domain (SID) is the amino acid sequence shared by all AHCY-1 fragments (prey)  
556 interacting with CHN-1. The confidence score of this binding (predicted biological score) is A  
557 (highest confidence). F) Co-immunoprecipitation of AHCY-1 and UFD-2 from young adult worms  
558 expressing CHN-1::FLAG using beads conjugated with anti-FLAG antibody. Protein samples were  
559 resolved via SDS-PAGE and immunoblotted with anti-AHCY-1, anti-FLAG, and anti-UFD-2  
560 antibodies. (The red boxes mark the protein band). G) Ubiquitylation of recombinant AHCY-1 was  
561 performed as indicated using recombinant CHN-1, UFD-2, DAF-21, HSP-1 in the presence of  
562 UBE2D1. Protein samples were resolved via SDS-PAGE and immunoblotted with anti-AHCY-1  
563 antibodies. H) Ubiquitylation of recombinant AHCY-1 was performed as indicated using  
564 recombinant UFD-2 and UBE2D1 E2. Protein samples were resolved via SDS-PAGE and  
565 immunoblotted with anti-AHCY-1 antibodies. Immunoblots representative of  $n = 3$  experiments  
566 are shown.

567

568 **STAR★METHODS**

569

570 **Lead Contact**

571

572 Further information and requests for reagents may be directed to and will be fulfilled by Wojciech  
573 Pokrzywa (wpokrzywa@iimcb.gov.pl).

574

575 **Materials Availability**

576

577 Plasmids generated by the authors will be distributed upon request to other researchers.

578

579 **Data a Availability**

580

581 The mass spectrometry proteomics data was deposited to the ProteomeXchange Consortium via  
582 the PRIDE partner repository with the dataset identifier PXD028023 (Perez-Riverol et al., 2019).

583

584 **Generation of recombinant proteins**

585

586 All recombinant proteins were produced using a bacterial expression system. CHN-1 and the CHN-  
587 1 variants were expressed and purified from Rosetta™ 2 (DE3) cells. UFD-2, HSP-1, DAF-21, and  
588 their variants were expressed and purified from BL21 Star™ (DE3) cells. Truncations and point  
589 mutations in the protein constructs were introduced using the Q5 Site-Directed Mutagenesis Kit  
590 (NEB, Cat#E0552S). Protein expression was induced using 0.4 mM IPTG at 22 °C for 16 hr.  
591 Respective induced cell pellets were harvested via centrifugation at 4000 rpm for 20 min at 4 °C.  
592 Cells were lysed in a lysis buffer (20 mM HEPES pH 8, NaCl 300 mM, 2 mM BME, protease  
593 inhibitor, and DNase) by sonication. After sonication, the supernatant and pellet fractions were  
594 separated via high-speed centrifugation at 14000 rpm for 1 hr at 22 °C. Tagged proteins were  
595 purified from the soluble fraction of the cell lysates using appropriate Ni-NTA or GST Hi-trap  
596 columns or chitin beads (NEB, Cat#E6901S). After removing the affinity tags, affinity-purified  
597 protein fractions were subjected to gel filtration chromatography (Hiload 16/600 Superdex S200,  
598 GE Healthcare) to obtain more than 95% pure protein fractions for use in subsequent biophysical  
599 and biochemical experiments. For the *in vitro* ubiquitylation reactions, we first generated a  
600 pTYB21-UFD-2 expression vector and purified tagless UFD-2 fraction using the intein cleavage  
601 site as per the manufacturer protocol (NEB Cat#E6901S). The lysis buffer used for purifying this  
602 variant contained HEPES 20mM, TritonX 0.1%, 5% glycerol, 500 mM NaCl, pH 8.0. To generate  
603 tagless CHN-1 and His-tagged CHN-1, we affinity-purified the proteins using Ni-NTA columns  
604 and then collected the dimeric fraction using size-exclusion chromatography (SEC). Furthermore,  
605 SUMO and the His-tag were cleaved using SUMO protease treatment (16 hr) at 4 degrees, and  
606 untagged CHN-1 was purified via SEC.

607

## 608 **Peptide microarray for protein-peptide interaction studies**

609  
610 This assay was performed by PEPperPRINT GmbH (<https://www.pepperprint.com/>). The CHN-1  
611 and UFD-2 sequences were elongated with neutral GSGSGSG linkers on the C- and N-termini to  
612 avoid truncated peptides. The elongated CHN-1 sequence was translated into 7, 10, and 13 amino  
613 acid peptides with peptide-peptide overlaps of 6, 9, and 12 amino acids. The elongated UFD-2  
614 sequence was translated into 7 and 13 amino acid peptides with peptide-peptide overlaps of 6 and  
615 12 amino acids. After peptide synthesis, all peptides were cyclized via a thioether linkage between  
616 a C-terminal cysteine and an appropriately modified N-terminus. The resulting conformational  
617 CHN-1 and UFD-2 peptide microarrays contained 813 and 1,986 different peptides printed in  
618 duplicate (1,626 and 3,972 peptide spots), respectively. The peptide array was framed by additional  
619 HA control peptides (YPYDVPDYAG, 68 spots for CHN-1 and 130 spots for UFD-2). Samples:  
620 His-tagged SUMO CHN-1, His-tagged SUMO and His-tagged UFD-2 proteins. Washing Buffer:  
621 TBS, pH 7.5 with 0.005% Tween 20; washing for 2 x 10 sec after each incubation step. Blocking  
622 Buffer: Rockland blocking buffer MB-070 (30 min before the first assay). Incubation Buffer: TBS,  
623 pH 8 with 10% Rockland blocking buffer MB-070, 10 mM HEPES, 150 mM NaCl and 0.005%  
624 Tween 20. Assay Conditions: Protein concentrations of 10 µg/mL and 100 µg/mL in incubation  
625 buffer; incubation for 16 h at 4 °C and shaking at 140 rpm. Secondary Antibody: Mouse anti-6x-  
626 His Epitope Tag DyLight680 (1.0 µg/mL); 45 min staining in incubation buffer at RT. Control  
627 Antibody: Mouse monoclonal anti-HA (12CA5) DyLight800 (0.5 µg/mL); 45 min staining in  
628 incubation buffer at RT. Scanner: LI-COR Odyssey Imaging System; scanning offset 0.65 mm,  
629 resolution 21 µm, scanning intensities of 7/7 (red = 700 nm/green = 800 nm). Microarray Data:  
630 Microarray Data Sumo Protein (PEP20205011547).xlsx, Microarray Data Sumo CHN-1 Protein  
631 (PEP20205011547).xlsx, Microarray Data UFD-2 Protein (PEP20205011547).xlsx. Microarray  
632 Identifier: 002413\_05 (CHN-1 microarray, four array copies for one-by-one assays) 002413\_07 &  
633 002413\_08 (UFD-2 microarray, two array copies for one-by-one assays).

634

## 635 **Ubiquitylation assays**

636  
637 *In vitro* assays were performed according to an earlier protocol (Hellerschmied et al., 2018). The  
638 reactions were run at 30 °C for 90 minutes using 60 µM Ubiquitin (Boston Biochem, Ub<sup>WT</sup> Cat#U-  
639 100H; Ub<sup>NoK</sup>, Cat#UM-NOK; Ub<sup>3KTR</sup>, Cat#UM-3KTR; Ub K48 only, Cat#UM-K480; Ub K63  
640 only, Cat#UM-K630) in the presence of 100 nM E1 (UBE1, Boston Biochem, Cat#E-304), 0.6 µM  
641 E2 (Boston Biochem, UBE2D1, Cat#E2-616; UBE2D2, Cat#E2-622; UBE2D3, Cat#E2-627;  
642 UBE2N/Uev1a, Cat#E2-664), E3 ligase (1 µM CHN-1 and variants or 0.7 µM UFD-2 and  
643 variants), E3 ligase reaction buffer (Boston Biochem, Cat#B-71), and Energy Regeneration  
644 Solution (Boston Biochem, Cat#B-10). For performing the *in vitro* reaction in the presence of both  
645 the CHN-1 and UFD-2 or His-tagged UFD-2<sup>P951A</sup>, proteins were first pre-incubated at 16 °C for 30  
646 min in the presence of E3 ligase reaction buffer. After that, the remaining reagents were added for  
647 the ubiquitylation reaction and incubated at 30 °C for the indicated time. For substrate  
648 ubiquitylation, *C. elegans* AH CY-1 was added as the substrate along with the other reagents and



649 mixed with pre-incubated CHN-1 or pre-incubated CHN-1/UFD-2 and incubated at 30 °C for 90  
650 mins. For performing the *in vitro* reaction in the presence of a chaperone, *C. elegans* 1 μM His-  
651 tagged HSP-1, His-tagged DAF-21, or other variants were pre-incubated with CHN-1 or CHN-  
652 1/UFD-2 at 16 °C for 30 min in the presence of 1x E3 ligase reaction buffer. After that, the  
653 remaining reagents were added for the reaction and incubated at 30 °C for 90 min. After the  
654 reaction, SDS-loading dye (Bio-rad, Cat#1610747), including β-mercaptoethanol (Sigma,  
655 Cat#M6250), was added to the entire reaction mix, and the samples were incubated at 95 °C for 5  
656 min. Samples were run in 12% SDS-PAGE gels and blotted with an antibody against the protein  
657 of interest.

658

## 659 **E2 discharge assays**

660

661 E2 discharging experimental protocol designed based on a modified method from Page et al., 2012.  
662 Discharging of increasing molar concentration (0.8, 1.6, 3.3, 5, 6.6 μM) of charged UBE2D1  
663 (Boston Biochem, UBE2D1-Ub, Cat#E2-800) was performed at 30 °C for 40 min in ubiquitin  
664 conjugation reaction buffer (Boston Biochem, Cat#B-70). Similarly, a time-dependent assay was  
665 performed using 3.3 μM UBE2D1-Ub at 30 °C for different time points (5, 10, 20, 30 mins) with  
666 equimolar concentrations (1 μM) of CHN-1, His-tagged UFD-2<sup>P951A</sup> and His-tagged HSP-1. The  
667 reaction was stopped by the addition of SDS-loading dye (Bio-Rad, Cat#1610747) without any  
668 reducing agent and incubation at 30 °C for 5 min. Samples were run in a 15% SDS-PAGE gel. For  
669 detecting the available UBE2D1-Ub in each condition, western blotting was performed using an  
670 anti-ubiquitin antibody. Normalized chemiluminescence intensity was obtained after maximum  
671 background subtraction from each lane.

672

## 673 **Western blotting and quantification**

674

675 Protein samples in SDS-loading dye (reducing/non-reducing) were run in 12% or 15% acrylamide  
676 gels using running buffer (25 mM Tris, 190 mM Glycine, 0.1% SDS) at 120 volts (constant). The  
677 wet transfer was done at a constant 200 mA for 2 hr at room temperature using transfer buffer (25  
678 mM Tris, 190 mM Glycine, 10% methanol, pH 8.3). Blots were then blocked with 5% skimmed  
679 milk in TBST (50 mM Tris, 150 mM NaCl, 0.1% Tween 20, pH 7.5) for 1 hr at room temperature.  
680 Blots were incubated with primary antibody prepared in 5% skimmed milk in TBST at 4 °C,  
681 overnight. The blots were then washed three times with TBST for 10 min each. Finally, the blots  
682 were incubated with secondary antibodies prepared in 5% skimmed milk in TBST for 1 hr at room  
683 temperature. The blots were imaged using a ChemiDoc<sup>TM</sup> Imaging System (Bio-Rad). All  
684 antibodies used in this study are listed in the resource table. We used Image Lab<sup>TM</sup> (version 6.0.0  
685 build 25) software for blot quantification using Image Lab and graph plotted using GraphPad Prism  
686 9. The bands appeared after probing with a particular antibody were marked in high sensitivity  
687 mode and quantified. Normalized chemiluminescence intensities were determined after maximum  
688 background subtraction from each lane.

689

## 690 **Enzyme-linked immunosorbent assay (ELISA)**

691  
692 2  $\mu\text{g/mL}$  of UFD-2, His-tagged DAF-21, and His-tagged HSP-1 in coating buffer (100 mM  
693  $\text{NaHCO}_3$ , 32 mM  $\text{Na}_2\text{CO}_3$ , pH 9.2) were immobilized on Nunc-Immuno plates for ELISA (Thermo  
694 Fisher Scientific, Cat#44-2404) overnight at 4 °C. Blocking was performed with 2% BSA for 1  
695 hr at 25 °C followed by washing with TBST (0.1% Tween 20). After incubation with increasing  
696 CHN-1 concentrations of for 1 hr at 16 °C, unbound CHN-1 was washed away by subsequent  
697 TBST washing steps. Interacting proteins were detected using an antibody against CHN-1 (1:5000  
698 dilution, overnight 4 °C), followed by TBST washing and the addition of an HRP-conjugated  
699 secondary antibody. After the final wash, 100  $\mu\text{L}$  of pnPP substrate (Alkaline Phosphatase Yellow-  
700 Sigma, Cat#P7998) was added in the dark. After 15 min, the reaction was stopped by adding 50  
701  $\mu\text{L}$  of 3M NaOH and the absorbance was measured at 450 nm.

## 703 **Modeling and Molecular Dynamics**

704  
705 CHN-1 model was generated by homology modeling using a Swiss model server (Waterhouse et  
706 al., 2018) with PDB ID 2F42 and 2C2L as the templates. The primary sequence of peptides used  
707 for docking on the CHN-1 dimer model was 628-640 HSP-1 (P09446) and 894-911 UFD-2  
708 (Q09349). The protein and peptide complex structures were subjected to an energy minimization  
709 strategy using pmem.cuda (Goetz et al., 2012; Salomon-Ferrer et al., 2013) from AMBER18 (Case  
710 et al., 2018). We used tLeap binary (part of AMBER18) for solvating the structures in an octahedral  
711 TIP3P water box with a 15 Å distance from the structure surface to the box edges, and closeness  
712 parameter of 0.75 Å. The system was neutralized and solvated in a solution of 150 mM NaCl.  
713 AMBER ff14SB force field was used (Maier et al., 2015) and simulations were carried out by  
714 equilibrating the system for 1ns (NPT), at 1 atm, 300K, followed by 10ns NPT for non-bonded  
715 interaction. The particle mesh Ewald (PME) method was used to treat the long-range electrostatic  
716 interactions. Hydrogen bonds were constrained using SHAKE algorithm and integration time-step  
717 at 2 fs. (Ryckaert et al., 1977).

## 719 **Hydrogen deuterium exchange mass spectrometry (HDX-MS)**

720  
721 Prior to HDX-MS reactions, a complex of CHN-1 (3 mg/ml) and His-tagged UFD-2 (2 mg/ml) was  
722 formed by mixing the proteins in a 1:1 molar ratio followed by incubation at 25 °C temperature for  
723 30 min. HDX-MS of CHN-1 and CHN-1 in complex with UFD-2 were performed at five time  
724 points during the incubation with deuterium (10 sec, 1 min, 5 min, 25 min, 2 hrs) in triplicate. 5  $\mu\text{L}$   
725 aliquots of protein were added to 45  $\mu\text{L}$  of deuterated buffer (10 mM HEPES, 150 mM NaCl in  
726 99.99%  $\text{D}_2\text{O}$ ; pH=8.0) at room temperature. The exchange reaction was quenched by moving the  
727 exchange aliquots to pre-cooled tubes (on ice) containing 10  $\mu\text{L}$  of quenching buffer (2 M glycine,  
728 4 M guanidine hydrochloride, 100 mM TCEP in 99.99%  $\text{D}_2\text{O}$ , pH 2.3). After quenching, samples  
729 were frozen immediately in liquid nitrogen and kept at -80 °C until mass spectrometry  
730 measurement. Samples were thawed directly before measurement and injected manually onto the

731 nano ACQUITY UPLC system equipped with HDX-MS Manager (Waters). Proteins were digested  
732 online on 2.1 mm x 20 mm columns with immobilized Nepenthesin-2 (AffiPro), for 1.5 min at 20  
733 °C and eluted with 0.07% formic acid in water at a flow rate of 200 µl/min. Digested peptides were  
734 passed directly to the ACQUITY BEH C18 VanGuard pre-column from which they were eluted  
735 onto the reversed-phase ACQUITY UPLC BEH C18 column (Waters) using a 6–40% gradient of  
736 acetonitrile in 0.01% of formic acid at a flow rate of 90 µl/min at 0.5 °C. Samples were measured  
737 on the SYNAPT-G2 HDX-MS instrument (Waters) in IMS mode. The instrument parameters for  
738 MS detection were as follows: ESI – positive mode; capillary voltage – 3 kV; sampling cone  
739 voltage – 35 V; extraction cone voltage – 3 V; source temperature – 80 °C; desolvation temperature  
740 –175 °C; and desolvation gas flow - 800 l/h. The CHN-1 peptide list was obtained using non-  
741 deuterated protein samples, processed as described above for HDX experiments, and measured in  
742 MSe mode. Peptides were identified using ProteinLynx Global Server Software (Waters). The  
743 HDX-MS experiment was analyzed using DynamX 3.0 (Waters) software. The PLGS peptide list  
744 was filtered by minimum intensity criteria – 3000 and minimal product per amino acid – 0.3. All  
745 MS spectra were inspected manually. Final data analysis was carried out using in-house HaDex  
746 software (Puchała et al., 2020). Differential deuterium exchange of residues was mapped to the  
747 model of CHN-1 generated using the 2C2L CHIP structure on the Swiss model server  
748 (<https://swissmodel.expasy.org/>).

749

#### 750 **Surface plasmon resonance (SPR)**

751

752 SPR-based interaction analysis was carried out at 25°C on a Biacore™ S200 instrument (GE  
753 Healthcare, Sweden). Recombinant purified His-tagged UFD-2 and His-tagged Ufd2p proteins  
754 were immobilized on NTA Biacore sensor Chips (Series S) at 20 µg/mL. Single-cycle kinetics  
755 studies were performed by passing increasing concentrations (0, 100, 200, 500, 1000 and 2000  
756 nM) of analyte M1 diUb conjugates (UbiQ, Cat#UbiQ-L01) in SPR buffer (10 mM HEPES, 150  
757 mM NaCl, 0.05% Tween 20, 0.1% BSA, 50 µM EDTA, pH 8.0). The runs for both proteins were  
758 carried out under identical conditions. All injections were compiled in the same sensorgram with  
759 the response unit (RU) on Y-axis versus time (sec) on the X-axis.

760

#### 761 **Preparation of *C. elegans* lysates and co-immunoprecipitation**

762

763 Worms were grown at 20 °C. For protein extraction, worms were collected in M9 buffer and lysed  
764 using a lysis buffer (1M KCl, 1M Tris-HCL pH 8.2, 1M MgCl<sub>2</sub>, 0.07% NP-40, 0.7% Tween-20,  
765 0.1% gelatine) with protease inhibitor (Roche, Cat# 11873580001) and in the presence of DUB  
766 inhibitor (Sigma-Aldrich, Cat#E3876). First, worms in lysis buffer were snap-frozen in liquid  
767 nitrogen. Next, the frozen samples were sonicated (40% amplitude, 5 cycles of 30 s pulses at 30 s  
768 intervals, Vibra-Cell™) on ice. Samples were centrifuged at 13,000 rpm for 15 min and the  
769 supernatants were collected. For co-immunoprecipitation, anti-DYKDDDDK (FLAG tag)  
770 magnetic beads (Pierce™ Anti-DYKDDDDK Magnetic Agarose, Cat#A36797) were used. 50 µl  
771 of anti-DYKDDDDK magnetic beads slurry were used for 200 µl of worm lysate. Lysate of CHN-

772 1::FLAG-expressing worms was used as the experimental sample and wild-type (N2) worms were  
773 used as a negative control. Worm lysates were incubated with equilibrated magnetic beads at 4 °C  
774 for 1 and 2 hr for UFD-2 and AHCY-1 pull down, respectively. After the desired incubations, the  
775 beads were washed three times using washing buffer (PBS with 100 mM NaCl). Samples were  
776 eluted via the addition of SDS-loading dye (Bio-rad, Cat#1610747) containing  $\beta$ -mercaptoethanol  
777 (Sigma, Cat#M6250) and boiling for 5 min.

778  
779 **RNA interference (RNAi)**  
780  
781 RNAi was performed using the standard RNAi feeding method and RNAi clones (Kamath and  
782 Ahringer, 2003). For experiments, NGM plates supplemented with 1 mM IPTG and 25  $\mu$ g/ $\mu$ L  
783 carbenicillin were seeded with HT115 *E. coli* expressing double-stranded RNA (dsRNA) against  
784 the gene of interest or, as a control, bacteria with the empty vector were used. Worms were placed  
785 on freshly prepared RNAi plates as age-synchronized L1 larvae.

786  
787 **Proteomics**  
788  
789 Protein digestion: For proteomic analysis, the following young adult strains were utilized: N2, *ufd-*  
790 *2(tm1380)*, *chn-1(by155)* and *ufd-2(tm1380); chn-1(by155)*. For lysis, 4% SDS in 100 mM HEPES  
791 pH = 8.5 was used, and the protein concentrations were determined. 50  $\mu$ g of protein was subjected  
792 for tryptic digestion. Proteins were reduced (10 mM TCEP) and alkylated (20 mM CAA) in the  
793 dark for 45 min at 45 °C. Samples were subjected to SP3-based digestion (Hughes et al., 2014).  
794 Washed SP3 beads (SP3 beads (Sera-Mag(TM) Magnetic Carboxylate Modified Particles  
795 (Hydrophobic), and Sera-Mag(TM) Magnetic Carboxylate Modified Particles (Hydrophilic)) were  
796 mixed equally, and 3  $\mu$ L of beads were added to each sample. Acetonitrile was added to a final  
797 concentration of 50%, and the samples were washed twice using 70% ethanol (200  $\mu$ L) on an in-  
798 house-made magnet. After an additional acetonitrile wash (200  $\mu$ L), 5  $\mu$ L of digestion solution (10  
799 mM HEPES pH 8.5 containing 0.5  $\mu$ g Trypsin (Sigma) and 0.5  $\mu$ g LysC (Wako)) was added to  
800 each sample and incubated overnight at 37 °C. Peptides were cleaned on a magnet using 2 x 200  
801  $\mu$ L acetonitrile washes. Peptides were eluted in 10  $\mu$ L of 5% DMSO in an ultrasonic bath for 10  
802 min. Formic acid and acetonitrile were added to final concentrations of 2.5% and 2%, respectively.  
803 Samples were frozen until LC-MS/MS analysis. Liquid chromatography and mass spectrometry:  
804 LC-MS/MS instrumentation consisted of a nLC 1200 coupled to a nanoelectrospray source to a  
805 QExactive HF-x (Thermo Fisher Scientific) mass spectrometer. Peptide separation was performed  
806 on an in-house-packed column (75  $\mu$ m inner diameter, 360  $\mu$ m outer diameter), and the column  
807 temperature was maintained at 50 °C using a column oven (PRSO-V2). The LC buffer system  
808 consisted out of 0.1% formic acid (A) and 0.1% formic acid in 80% acetonitrile (B). Peptides were  
809 separated using a 90 min gradient applying a linear gradient for 70 min from 7 to 29 % B and then  
810 ramped to 65% B within 10 min, followed by a linear increase to 95% B within 5 min. 95% B was  
811 held for 5 min. Before each run, the column was re-equilibrated to 0%B. The mass spectrometer  
812 operated in a data-dependent acquisition mode targeting the top 22 peaks for collision-induced

813 fragmentation and MS2 spectra acquisition. MS1 spectra were acquired in a scan range from 350  
814 to 1650 m/z allowing a maximum injection time of 20 ms for an AGC target of 3e6. Spectra were  
815 acquired at a resolution of 60,000 (at 200 m/z). Ions were isolated in an isolation window of 1.3  
816 m/z using an AGC target of 1e6 and a maximum injection time of 22ms. Spectra were acquired at  
817 a resolution of 15,000. The scan range for the MS2 spectra was set to 200–2000 m/z. The  
818 normalized collision energy was 28. Dynamic exclusion was set to 20 s. Data analysis: Acquired  
819 raw files were correlated to the Uniprot reference *C. elegans* proteome (downloaded: 06.2018)  
820 using MaxQuant (1.5.3.8) (Cox and Mann, 2008) and the implemented Andromeda search engine  
821 (Cox et al., 2011). Label-free quantification and matching between runs were enabled using default  
822 settings. Carbamidomethylation of cysteine residues was set as a fixed modification. Oxidation of  
823 methionine residues and acetylation of protein N-termini were defined as variable modifications.  
824 FDR was controlled using the implemented revert algorithm to 1% at the protein and the peptide-  
825 spectrum match (PSM). To identify significantly changed proteins, we performed a one-way  
826 analysis of variance (ANOVA) correcting for multiple testing using a permutation-based approach  
827 (FDR < 0.05, # permutations: 500).

828

## 829 **Lipidomics**

830

831 The following young adult strains were utilized for lipidomic analysis: N2 (wild-type), *ufd-*  
832 *2(tm1380)*, *chn-1(by155)*. Lipid extraction: Lipids from a homogenized sample comprising 15 000  
833 worms were extracted using the Folch method as follows: 200  $\mu$ L of methanol was added to each  
834 sample followed by 10 s of vortexing. Next, 500  $\mu$ L of chloroform was added, followed by 10 s  
835 vortexing. This was followed by the addition of 200  $\mu$ L of water to each sample to induce phase  
836 separation, following by vortexing for 20 s. The samples were then kept in the cold for 10 min. The  
837 samples were then centrifuged at 14,500 rpm for 10 min. The bottom layer was then pipetted out,  
838 and the solvent was dried under a stream of nitrogen. Prior to LC-MS analysis, the lipid extract  
839 was reconstituted in 200  $\mu$ L of 1:1 isopropanol:methanol solution. LC-MS analysis: LC-MS  
840 analysis was performed as previously described (Nature Methods volume 14, pages 57–60 (2017)).  
841 Briefly, lipid extracts were separated on a Kinetex C18 2.1 x 100 mm, 2.6  $\mu$ m column  
842 (Phenomenex, Aschaffenburg, De). Separation was achieved via gradient elution in a binary  
843 solvent, Vanquish UHPLC (Thermo Scientific, Bremen, DE). Mobile Phase A consisted of  
844 ACN:H<sub>2</sub>O (60:40), while mobile phase B consisted of IPA:ACN (90:10). For positive ionization,  
845 the mobile phases were modified with 10 mM ammonium formate and 0.1% formic acid, while for  
846 the negative ionization mode, the mobile phases were modified with 5 mM ammonium acetate and  
847 0.1% acetic acid. A flow rate of 260  $\mu$ L/min was used for separation, and the column and sample  
848 tray were held constant at 30 °C and 4 °C, respectively. 2  $\mu$ L of each sample was injected onto the  
849 LC column. MS Instrumentation: MS analysis was performed on a Q-Exactive Plus Mass  
850 Spectrometer (Thermo Scientific, Bremen, DE) equipped with a heated electrospray ionization  
851 probe. In both the positive and negative ionization modes, the S-Lens RF level was set to 65, and  
852 the capillary temperature was set to 320 °C, and the sheath gas flow was set to 30 units and the  
853 auxiliary gas was set to 5 units. The spray voltage was set to 3.5 kV in the negative ionization mode

854 and 4.5 kV in the positive ionization mode. In both modes, full scan mass spectra (scan range m/z  
855 100–1500, R=35K) were acquired along with data-dependent (DDA) MS/MS spectra of the five  
856 most abundant ions. DDA MS/MS spectra were acquired using normalized collision energies of  
857 30, 40, and 50 units (R= 17.5K and an isolation width = 1 m/z). The instrument was controlled  
858 using Xcalibur (version 4.0). Data analysis and lipid annotation: Progenesis Q1, version 2.0 (Non-  
859 Linear Dynamics, A Waters Company, Newcastle upon Tyne, UK) was used for peak picking and  
860 chromatographic alignment of all samples, with a pooled sample used as a reference. Lipids were  
861 annotated using the Progenesis Metascope Basic Lipids the LipidBlast databases with  
862 consideration made only of compounds that had MS/MS data. In both databases, the precursor ion  
863 tolerance was set to 10 ppm, and the fragmentation ion tolerance was set to 15 ppm. Putative lipid  
864 identifications were based on manual curation of database matches with fragmentation scores  
865 >10%.

866

### 867 **Fluorescent labeling of lipids in *C. elegans***

868

869 Lipid content in young adult worms was determined by RediStain™ WormDye Lipid Green  
870 (NemaMetrix, Cat#DYE9439) staining, according to the manufacturer's protocol with incubation  
871 for 30 mins at room temperature with shaking. Working dye concentration: 1 µl of dye/200 µl of  
872 M9 buffer. Worms were protected from light, and several washes in M9 buffer were performed  
873 after staining. Immediately after that, imaging was performed on a Nikon SMZ25 microscope after  
874 immobilizing worms with tetramizole. Data analysis: Image processing was performed with  
875 ImageJ (Fiji) using Binary Mask and Particle Analysis Procedure with background signal  
876 subtraction. The graphs were plotted using GraphPad Prism 9.

877

### 878 **Yeast two-hybrid screening**

879

880 Yeast two-hybrid screening was performed by Hybrigenics Services ([http://www.hybrigenics-](http://www.hybrigenics-services.com)  
881 [services.com](http://www.hybrigenics-services.com)). The coding sequence for *C. elegans* CHN-1 (NM\_059380.5, aa 1–266) was PCR-  
882 amplified and cloned into pB27 as a C-terminal fusion to LexA (LexA-CHN-1). The construct was  
883 checked by sequencing the entire insert and used as a bait to screen a random-primed *C. elegans*  
884 mixed-stage cDNA library constructed into pP6. pB27 and pP6 were derived from the original  
885 pBTM116 (Vojtek and Hollenberg, 1995) and pGADGH (Bartel et al., 1993) plasmids,  
886 respectively. 61 million clones (6-fold the complexity of the library) were screened using a mating  
887 approach with YHGX13 (Y187 ade2-101::loxP-kanMX-loxP, mat<sup>+</sup>) and L40<sup>+</sup>Gal4 (mata) yeast  
888 strains as previously described (Fromont-Racine et al., 1997). 202 His<sup>+</sup> colonies were selected on  
889 a medium lacking tryptophan, leucine, and histidine and supplemented with 50 mM 3-  
890 aminotriazole to prevent bait autoactivation. The prey fragments of the positive clones were  
891 amplified by PCR and sequenced at their 5' and 3' junctions. The resulting sequences were used to  
892 identify the corresponding interacting proteins in the GenBank database (NCBI) using a fully  
893 automated procedure. A confidence score (PBS, for Predicted Biological Score) was attributed to  
894 each interaction as previously described (Formstecher et al., 2005). The PBS relies on two different

895 levels of analysis. First, a local score considers the redundancy and independence of prey fragments  
896 and the distribution of reading frames and stop codons in overlapping fragments. Second, a global  
897 score considers the interactions found in all of the screens performed by Hybrigenics using the  
898 same library. This global score represents the probability of interaction being nonspecific. The  
899 scores were divided into four categories for practical use, from A (highest confidence) to D (lowest  
900 confidence). A fifth category (E) flags explicit interactions involving highly connected prey  
901 domains previously found several times in screens performed on libraries derived from the same  
902 organism. Finally, several of these highly connected domains were confirmed as false positives  
903 and were tagged as F. PBS scores have been shown to positively correlate with the biological  
904 significance of interactions (Rain et al., 2001; Wojcik et al., 2002).

905

## 906 **Acknowledgments**

907

908 We thank the *Caenorhabditis* Genetics Center (funded by the NIH National Center for Research  
909 Resources, P40 OD010440) for strains, Addgene for plasmids and Katarzyna Prokop and Marta  
910 Niklewicz for technical assistance. We thank Vishnu Balaji and Gabriele Stellbrink of the Hoppe  
911 laboratory for discussions and technical support and members of Pokrzywa laboratory for  
912 discussions and comments on the manuscript.

913

## 914 **Funding**

915

916 Work in the W.P. laboratory was funded by the Foundation for Polish Science co-financed by the  
917 European Union under the European Regional Development Fund (grant POIR.04.04.00-00-  
918 5EAB/18-00) and additionally supported by Polish National Science Center (grant UMO-  
919 2016/23/B/NZ3/00753). The equipment used for HDX-MS was sponsored by the National  
920 Multidisciplinary Laboratory of Functional Nanomaterials (POIGT.02.02.00-00-025/09-00). Work  
921 in the T.H. laboratory was funded by the Deutsche Forschungsgemeinschaft (DFG, German  
922 Research Foundation) under Germany's Excellence Strategy – EXC 2030 – 390661388, FKZ:  
923 ZUK81/1 and by the European Research Council (ERC-CoG-616499) to T.H. Diese Arbeit wurde  
924 von der Deutschen Forschungsgemeinschaft (DFG) im Rahmen der deutschen Exzellenzstrategie  
925 - EXC 2030 – 390661388, FKZ: ZUK81 / 1 und vom Europäischen Forschungsrat (ERC-CoG-  
926 616499) gefördert. Work in M.K. laboratory was supported by the German Research Foundation  
927 (DFG) as part of the Excellence Strategy EXC 2030-390661388. C.J.C. and U.S. were funded by  
928 National Institute of Health grants R01-GM097082.

929

## 930 **Author contributions**

931

932 The project was initiated in the laboratory of T.H. A.D., P.T., N.S., K.B., and W.P. designed and  
933 conducted experiments. U.S. and C.J.C. performed structural modeling and simulation analysis.  
934 R.M.G. performed the lipidomic analysis. N.A.S performed the bioinformatic analyses. H.N. and  
935 M.K. performed the proteomic analyses. K.D, D.C, M.D. performed the HDX-MS studies. W.P.

936 (with input from M.N.) conceived the project and supervised the study. W.P. (with input from  
 937 M.N.) secured the funding. W.P. and A.D. wrote the manuscript with input from M.N, T.H and  
 938 C.J.C. The authors declare no competing financial interests.

939  
 940

941 **TABLE S1. List of constructs and oligonucleotides used to generate them**  
 942

Construct	Primer Sequence (5'-3')
pTYB21-MBP::Intein-UFD-2	Forward: GGTGGTTGCTCTTCCAACATGATTGAAGACGAGAAAGCAGG
	Reverse: GGTGGTCTGCAGTCATTATTTCTTTGAATTTCTTT
pET-6xHis::SUMO-CHN-1 <sup>Δ110</sup>	Forward: ATTGAGAACGCCCTCAAAC
	Reverse: GCTAGCTAGACCACCAATC
pET-6xHis::SUMO-CHN-1 <sup>Δ87</sup>	Forward: TACAGTGAAGCAATAAGCTG
	Reverse: GCTAGCTAGACCACCAATC
pET-6xHis::SUMO-CHN-1 <sup>Δ95</sup>	Forward: TCAAAGCGCTCTACCAT
	Reverse: GCTAGCTAGACCACCAATC
pET-21a-VSV-HSP-1 <sup>EEVD</sup> ::6xHis	Forward: ATCGAGGAGTACGACGCGGCC
	Reverse: GGCCGCGTCGTA CTCTCGAT
pET-21a-VSV-HSP-1ΔEEVD::6xHis	Forward: GCGGCCGCACTCGAG
	Reverse: TCCTCCGGCGGCTCCTCC
pET-21a-6xHis::DAF-21ΔEEVD	Forward: TAATGAGGATCCGAATTCGAG
	Reverse: CTCAGCTCCCTCAATCTT
pET-6xHis::SUMO-CHN-1 <sup>R230A</sup>	Forward: TCCAGTCACAGCAAAACCACTTAC
	Reverse: TCGAAATGGCCAATTCTTC

943



## KEY RESOURCES TABLE

REAGENT or RESOURCE	SOURCE	IDENTIFIER
<b>Chemicals, Peptides, and Recombinant Proteins</b>		
UBE1	Boston Biochem	Cat#E-304
UBE2D1	Boston Biochem	Cat#E2-616
UBE2D2	Boston Biochem	Cat#E2-622
UBE2D3	Boston Biochem	Cat#E2-627
UBE2N/Uev1a	Boston Biochem	Cat#E2-664
10X E3 Ligase Reaction Buffer	Boston Biochem	Cat#B-71
10X Ubiquitin conjugation Reaction Buffer	Boston Biochem	Cat#B-70
10X Energy Regeneration Solution	Boston Biochem	Cat#B-10
Ubiquitin	Boston Biochem	Cat#U-100H
UbNoK	Boston Biochem	Cat#UM-NOK
Ub3KTR	Boston Biochem	Cat#UM-3KTR
UbK48only	Boston Biochem	Cat#UM-K480
UbK63only	Boston Biochem	Cat#UM-K630
M1linked- linear ubiquitin	UbiQ	Cat#UbiQ-L01
UBE2D1 ubiquitin charged	Boston Biochem	Cat#E2-800
N-Ethylmaleimide	Sigma-Aldrich	Cat#E3876
cOmplete™, EDTA-free Protease Inhibitor Cocktail	Roche	Cat# 11873580001
MG-132	Selleckchem	Cat#S2619
Alkaline Phosphatase Yellow (pNPP) Liquid Substrate	Sigma-Aldrich	Cat#P7998
Q5 Site-Directed Mutagenesis Kit	NEB	Cat#E0552S
4x Laemmli Sample Buffer	Bio-Rad	Cat#1610747
β-Mercaptoethanol	Sigma-Aldrich	Cat#M6250
Dynabeads™ Co-Immunoprecipitation Kit	Invitrogen	Cat#14321D
Pierce™ Anti-DYKDDDDK Magnetic Agarose	Invitrogen	Cat#A36797
RediStain™ WormDye Lipid Green	NemaMetrix	Cat#DYE9439
IMPACT™ Kit	NEB	Cat#E6901S
AHCY-1::6xHis	This study	N/A
CHN-1	This study	N/A
6xHis::SUMO::CHN-1	This study	N/A
CHN-1 <sup>Δ110</sup>	This study	N/A
CHN-1 <sup>Δ87</sup>	This study	N/A
CHN-1 <sup>Δ95</sup>	This study	N/A
CHN-1 <sup>R230A</sup>	This study	N/A
UFD-2	This study	N/A
6xHis::UFD-2	This study	N/A
6xHis::UFD-2 <sup>P951A</sup>	(Ackermann et al., 2016)	N/A
6xHis::UFD-2 <sup>ΔUbox</sup>	This study	N/A

6xHis::Ufd2p	This study	N/A
HSP-1::6xHis	This study	N/A
6xHis::DAF-21	This study	N/A
HSP-1 $\Delta$ EEVD::6xHis	This study	N/A
6xHis::DAF-21 $\Delta$ EEVD	This study	N/A
HSP-1 <sup>EEVD</sup> ::6xHis	This study	N/A
<b>Antibodies</b>		
Anti-CHN-1 antibody	(Tawo et al., 2017)	N/A
Anti-UFD-2 antibody	(Ackermann et al., 2016)	N/A
Anti-AHCY-1 antibody	This study	N/A
Anti-Ubiquitin antibody	Cell signaling Technology	Cat#3936s
Anti-Histidine antibody	Santa Cruz Biotechnology, Inc.	Cat#SC-53073
Anti-GST antibody	Sigma-Aldrich	Cat#G1160
<b>Bacterial Strains</b>		
<i>E. coli</i> RNAi feeding strain	Caenorhabditis Genetics Center	HT115(DE3)
<i>E. coli</i> feeding strain	Caenorhabditis Genetics Center	OP50
Ahringer RNAi library	Source BioScience	<i>C. elegans</i> RNAi Collection (Ahringer)
Rosetta <sup>TM</sup> 2 (DE3)	Novagen	Cat#71400
BL21 Star <sup>TM</sup> (DE3)	Thermo Fisher Scientific	Cat#C601003
Top10	Thermo Fisher Scientific	Cat#C4040
<b>Oligonucleotides</b>		
For the list of oligonucleotides, see Table S1	N/A	N/A
<b>Plasmid construct</b>		
pET28a-6xHis::Ufd2p	(Liu et al., 2017)	N/A
pET-6xHis::SUMO::CHN-1	This study	N/A
pET28a-6xHis::UFD-2	This study	N/A
pLATE31-AHCY-1::6xHis	This study	N/A
pET21a-VSV::HSP-1::6xHis	This study	N/A
pET21a-6xHis::DAF-21	This study	N/A
pTYB21-MBP::Intein-UFD-2	This study	N/A
pET-6xHis::SUMO-CHN-1 $\Delta$ 110	This study	N/A
pET-6xHis::SUMO-CHN-1 $\Delta$ 87	This study	N/A

pET-6xHis::SUMO-CHN-1 <sup>Δ95</sup>	This study	N/A
pET-21a-VSV-HSP-1 <sup>EEYD</sup> ::6xHis	This study	N/A
pET-21a-VSV-HSP-1 <sup>ΔEEVD</sup> ::6xHis	This study	N/A
pET-21a-6xHis::DAF-21 <sup>ΔEEVD</sup>	This study	N/A
pET-6xHis::SUMO-CHN-1 <sup>R230A</sup>	This study	N/A
<b>Experimental Models: Organisms/Strains</b>		
<i>C. elegans</i> : Bristol (N2) strain as wild-type	CGC	N/A
<i>C. elegans</i> : chn-1(by155)I	CGC	WormBase ID: WBVar00000641
<i>C. elegans</i> : unc-119(ed4)III; hhIs136[unc-119(+); chn-1p::chn-1::FLAG]	(Tawo et al., 2017)	N/A
<i>C. elegans</i> : ufd-2(tm1380)II	CGC	WormBase ID: WBVar00250374
<i>C. elegans</i> : chn-1(by155)I; ufd-2(tm1380)II	This study	N/A
<b>Software and Algorithms</b>		
Graph Pad Prism	Graph Pad Software, Inc.	www.graphpad.com
Image Lab <sup>TM</sup> Version 6.0.0 build 25	Bio-Rad Laboratories, Inc.	www.bio-rad.com/de-de/product/image-lab-software?ID=KRE6P5E8Z
ImageJ 1.53c	Wayne Rasband, NIH, USA	www.imagej.nih.gov/ij
<b>Materials</b>		
Nunc MaxiSorp <sup>TM</sup> flat-bottom	Thermo Fisher Scientific	Cat#44-2404
Hiload 16/600 Superdex S200	GE Healthcare	Cat#GE28-9893-35

944  
945  
946  
947

## REFERENCES

948 Ackermann, L., Schell, M., Pokrzywa, W., Kevei, É., Gartner, A., Schumacher, B., and Hoppe,  
949 T. (2016). E4 ligase-specific ubiquitination hubs coordinate DNA double-strand-break repair and  
950 apoptosis. *Nat. Struct. Mol. Biol.*  
951 Ballinger, C.A., Connell, P., Wu, Y., Hu, Z., Thompson, L.J., Yin, L.-Y., and Patterson, C.  
952 (1999). Identification of CHIP, a Novel Tetratricopeptide Repeat-Containing Protein That  
953 Interacts with Heat Shock Proteins and Negatively Regulates Chaperone Functions. *Mol. Cell.*  
954 *Biol.*  
955 Bartel, P., Chien, C.T., Sternglanz, R., and Fields, S. (1993). Elimination of false positives that  
956 arise in using the two-hybrid system. *Biotechniques.*  
957 Bhuripanyo, K., Wang, Y., Liu, X., Zhou, L., Liu, R., Duong, D., Zhao, B., Bi, Y., Zhou, H.,

958 Chen, G., et al. (2018). Identifying the substrate proteins of U-box E3s E4B and CHIP by  
959 orthogonal ubiquitin transfer. *Sci. Adv.*

960 Buetow, L., and Huang, D.T. (2016). Structural insights into the catalysis and regulation of E3  
961 ubiquitin ligases. *Nat. Rev. Mol. Cell Biol.*

962 Cantoni, G.L. (1975). Biological methylation: selected aspects. *Annu. Rev. Biochem.*

963 Case, D.A., Ben-Shalom, I.Y., Brozell, S.R., Cerutti, D.S., Cheatham III, T.E., Cruzeiro, V.W.D.,  
964 Darden, T.A., Duke, R.E., Ghoreishi, D., and Gilson, M.K. (2018). Amber 2018; 2018. Univ.  
965 California, San Fr.

966 Cox, J., and Mann, M. (2008). MaxQuant enables high peptide identification rates, individualized  
967 p.p.b.-range mass accuracies and proteome-wide protein quantification. *Nat. Biotechnol.*

968 Cox, J., Neuhauser, N., Michalski, A., Scheltema, R.A., Olsen, J. V., and Mann, M. (2011).  
969 Andromeda: A peptide search engine integrated into the MaxQuant environment. *J. Proteome*  
970 *Res.*

971 Faull, S. V., Lau, A.M.C., Martens, C., Ahdash, Z., Hansen, K., Yebenes, H., Schmidt, C.,  
972 Beuron, F., Cronin, N.B., Morris, E.P., et al. (2019). Structural basis of Cullin 2 RING E3 ligase  
973 regulation by the COP9 signalosome. *Nat. Commun.*

974 Formstecher, E., Aresta, S., Collura, V., Hamburger, A., Meil, A., Trehin, A., Reverdy, C., Betin,  
975 V., Maire, S., Brun, C., et al. (2005). Protein interaction mapping: A Drosophila case study.  
976 *Genome Res.*

977 Fromont-Racine, M., Rain, J.C., and Legrain, P. (1997). Toward a functional analysis of the yeast  
978 genome through exhaustive two- hybrid screens. *Nat. Genet.*

979 Gazda, L., Pokrzywa, W., Hellerschmied, D., Löwe, T., Forné, I., Mueller-Planitz, F., Hoppe, T.,  
980 and Clausen, T. (2013). The myosin chaperone UNC-45 is organized in tandem modules to  
981 support myofilament formation in *C. elegans*. *Cell.*

982 Goetz, A.W., Williamson, M.J., Xu, D., Poole, D., Grand, S.L., and Walker, R.C. (2012). Routine  
983 microsecond molecular dynamics simulations with AMBER - part 1: Generalized Born. *J. Chem.*  
984 *Theory Comput.*

985 Graf, C., Stankiewicz, M., Nikolay, R., and Mayer, M.P. (2010). Insights into the conformational  
986 dynamics of the E3 ubiquitin ligase CHIP in complex with chaperones and E2 enzymes.  
987 *Biochemistry.*

988 Hänzelmann, P., Stingele, J., Hofmann, K., Schindelin, H., and Raasi, S. (2010). The yeast E4  
989 ubiquitin ligase Ufd2 interacts with the ubiquitin-like domains of Rad23 and Dsk2 via a novel  
990 and distinct ubiquitin-like binding domain. *J. Biol. Chem.*

991 Hatakeyama, S., Yada, M., Matsumoto, M., Ishida, N., and Nakayama, K.I. (2001). U Box  
992 Proteins as a New Family of Ubiquitin-Protein Ligases. *J. Biol. Chem.*

993 Hellerschmied, D., Roessler, M., Lehner, A., Gazda, L., Stejskal, K., Imre, R., Mechtler, K.,  
994 Dammermann, A., and Clausen, T. (2018). UFD-2 is an adaptor-assisted E3 ligase targeting  
995 unfolded proteins. *Nat. Commun.*

996 Hoppe, T., Cassata, G., Barral, J.M., Springer, W., Hutagalung, A.H., Epstein, H.F., and  
997 Baumeister, R. (2004). Regulation of the myosin-directed chaperone UNC-45 by a novel E3/E4-  
998 multiubiquitylation complex in *C. elegans*. *Cell.*

999 Houde, D., Berkowitz, S.A., and Engen, J.R. (2011). The utility of hydrogen/deuterium exchange  
1000 mass spectrometry in biopharmaceutical comparability studies. *J. Pharm. Sci.*

1001 Huerta-Cepas, J., Szklarczyk, D., Heller, D., Hernández-Plaza, A., Forslund, S.K., Cook, H.,  
1002 Mende, D.R., Letunic, I., Rattei, T., Jensen, L.J., et al. (2019). EggNOG 5.0: A hierarchical,  
1003 functionally and phylogenetically annotated orthology resource based on 5090 organisms and  
1004 2502 viruses. *Nucleic Acids Res.*

1005 Hughes, C.S., Foehr, S., Garfield, D.A., Furlong, E.E., Steinmetz, L.M., and Krijgsveld, J.  
1006 (2014). Ultrasensitive proteome analysis using paramagnetic bead technology. *Mol. Syst. Biol.*  
1007 Jiang, J., Ballinger, C.A., Wu, Y., Dai, Q., Cyr, D.M., Höhfeld, J., and Patterson, C. (2001).  
1008 CHIP is a U-box-dependent E3 ubiquitin ligase: Identification of Hsc70 as a target for  
1009 ubiquitylation. *J. Biol. Chem.*  
1010 Joshi, V., Amanullah, A., Upadhyay, A., Mishra, R., Kumar, A., and Mishra, A. (2016). A decade  
1011 of boon or burden: What has the chip ever done for cellular protein quality control mechanism  
1012 implicated in neurodegeneration and aging? *Front. Mol. Neurosci.*  
1013 Kamadurai, H.B., Qiu, Y., Deng, A., Harrison, J.S., MacDonald, C., Actis, M., Rodrigues, P.,  
1014 Miller, D.J., Souphron, J., Lewis, S.M., et al. (2013). Mechanism of ubiquitin ligation and lysine  
1015 prioritization by a HECT E3. *Elife.*  
1016 Kamath, R.S., and Ahringer, J. (2003). Genome-wide RNAi screening in *Caenorhabditis elegans*.  
1017 *Methods.*  
1018 Kerscher, O., Felberbaum, R., and Hochstrasser, M. (2006). Modification of proteins by ubiquitin  
1019 and ubiquitin-like proteins. *Annu. Rev. Cell Dev. Biol.*  
1020 Koegl, M., Hoppe, T., Schlenker, S., Ulrich, H.D., Mayer, T.U., and Jentsch, S. (1999). A novel  
1021 ubiquitination factor, E4, is involved in multiubiquitin chain assembly. *Cell.*  
1022 Komander, D. (2009). The emerging complexity of protein ubiquitination. *Biochem. Soc. Trans.*  
1023 Liao, Y., Wang, J., Jaehnig, E.J., Shi, Z., and Zhang, B. (2019). WebGestalt 2019: gene set  
1024 analysis toolkit with revamped UIs and APIs. *Nucleic Acids Res.*  
1025 Liu, J., and Nussinov, R. (2011). Flexible cullins in cullin-RING E3 ligases allosterically regulate  
1026 ubiquitination. *J. Biol. Chem.*  
1027 Liu, C., Liu, W., Ye, Y., and Li, W. (2017). Ufd2p synthesizes branched ubiquitin chains to  
1028 promote the degradation of substrates modified with atypical chains. *Nat. Commun.*  
1029 Maier, J.A., Martinez, C., Kasavajhala, K., Wickstrom, L., Hauser, K.E., and Simmerling, C.  
1030 (2015). ff14SB: Improving the Accuracy of Protein Side Chain and Backbone Parameters from  
1031 ff99SB. *J. Chem. Theory Comput.*  
1032 Murata, S., Minami, Y., Minami, M., Chiba, T., and Tanaka, K. (2001). CHIP is a chaperone-  
1033 dependent E3 ligase that ubiquitylates unfolded protein. *EMBO Rep.*  
1034 Narayan, V., Landré, V., Ning, J., Hernychova, L., Muller, P., Verma, C., Walkinshaw, M.D.,  
1035 Blackburn, E.A., and Ball, K.L. (2015). Protein-protein interactions modulate the docking-  
1036 dependent E3-ubiquitin ligase activity of carboxy-terminus of Hsc70-interacting protein (CHIP).  
1037 *Mol. Cell. Proteomics.*  
1038 Nikolay, R., Wiederkehr, T., Rist, W., Kramer, G., Mayer, M.P., and Bukau, B. (2004).  
1039 Dimerization of the Human E3 Ligase CHIP via a Coiled-coil Domain Is Essential for Its  
1040 Activity. *J. Biol. Chem.*  
1041 Notredame, C., Higgins, D.G., and Heringa, J. (2000). T-coffee: A novel method for fast and  
1042 accurate multiple sequence alignment. *J. Mol. Biol.*  
1043 Page, R.C., Pruneda, J.N., Amick, J., Klevit, R.E., and Misra, S. (2012). Structural insights into  
1044 the conformation and oligomerization of e2~ubiquitin conjugates. *Biochemistry.*  
1045 Palmer, J.L., and Abeles, R.H. (1976). Mechanism for enzymatic thioether formation.  
1046 Mechanism of action of S-adenosylhomocysteinase. *J. Biol. Chem.*  
1047 Palmer, J.L., and Abeles, R.H. (1979). The mechanism of action of S-adenosylhomocysteinase. *J.*  
1048 *Biol. Chem.*  
1049 Paul, I., and Ghosh, M.K. (2014). The E3 ligase CHIP: Insights into its structure and regulation.  
1050 *Biomed Res. Int.*  
1051 Perez-Riverol, Y., Csordas, A., Bai, J., Bernal-Llinares, M., Hewapathirana, S., Kundu, D.J.,

1052 Inuganti, A., Griss, J., Mayer, G., Eisenacher, M., et al. (2019). The PRIDE database and related  
1053 tools and resources in 2019: Improving support for quantification data. *Nucleic Acids Res.* *47*,  
1054 D442–D450.

1055 Puchała, W., Burdukiewicz, M., Kistowski, M., Dąbrowska, K.A., Badaczewska-Dawid, A.E.,  
1056 Cysewski, D., and Dadlez, M. (2020). HaDeX: An R package and web-server for analysis of data  
1057 from hydrogen-deuterium exchange mass spectrometry experiments. *Bioinformatics*.

1058 Rain, J.C., Selig, L., De Reuse, H., Battaglia, V., Reverdy, C., Simon, S., Lenzen, G., Petel, F.,  
1059 Wojcik, J., Schächter, V., et al. (2001). The protein-protein interaction map of *Helicobacter*  
1060 *pylori*. *Nature*.

1061 Richly, H., Rape, M., Braun, S., Rumpf, S., Hoegge, C., and Jentsch, S. (2005). A series of  
1062 ubiquitin binding factors connects CDC48/p97 to substrate multiubiquitylation and proteasomal  
1063 targeting. *Cell*.

1064 Ryckaert, J.P., Ciccotti, G., and Berendsen, H.J.C. (1977). Numerical integration of the cartesian  
1065 equations of motion of a system with constraints: molecular dynamics of n-alkanes. *J. Comput.*  
1066 *Phys.*

1067 Salomon-Ferrer, R., Götz, A.W., Poole, D., Le Grand, S., and Walker, R.C. (2013). Routine  
1068 microsecond molecular dynamics simulations with AMBER on GPUs. 2. Explicit solvent particle  
1069 mesh ewald. *J. Chem. Theory Comput.*

1070 Scheufler, C., Brinker, A., Bourenkov, G., Pegoraro, S., Moroder, L., Bartunik, H., Hartl, F.U.,  
1071 and Moarefi, I. (2000). Structure of TPR domain-peptide complexes: Critical elements in the  
1072 assembly of the Hsp70-Hsp90 multichaperone machine. *Cell*.

1073 Soss, S.E., Yue, Y., Dhe-Paganon, S., and Chazin, W.J. (2011). E2 conjugating enzyme  
1074 selectivity and requirements for function of the E3 ubiquitin ligase CHIP. *J. Biol. Chem.*

1075 Tawo, R., Pokrzywa, W., Kevei, É., Akyuz, M.E., Balaji, V., Adrian, S., Höhfeld, J., and Hoppe,  
1076 T. (2017). The Ubiquitin Ligase CHIP Integrates Proteostasis and Aging by Regulation of Insulin  
1077 Receptor Turnover. *Cell*.

1078 Tehlivets, O. (2011). Homocysteine as a Risk Factor for Atherosclerosis: Is Its Conversion to S -  
1079 Adenosyl- L -Homocysteine the Key to Deregulated Lipid Metabolism? . *J. Lipids*.

1080 Di Tommaso, P., Moretti, S., Xenarios, I., Oorbitg, M., Montanyola, A., Chang, J.M., Taly, J.F.,  
1081 and Notredame, C. (2011). T-Coffee: A web server for the multiple sequence alignment of  
1082 protein and RNA sequences using structural information and homology extension. *Nucleic Acids*  
1083 *Res.*

1084 Visram, M., Radulovic, M., Steiner, S., Malanovic, N., Eichmann, T.O., Wolinski, H.,  
1085 Rechberger, G.N., and Tehlivets, O. (2018). Homocysteine regulates fatty acid and lipid  
1086 metabolism in yeast. *J. Biol. Chem.*

1087 Vojtek, A.B., and Hollenberg, S.M. (1995). Ras-Raf Interaction: Two-Hybrid Analysis. *Methods*  
1088 *Enzymol.*

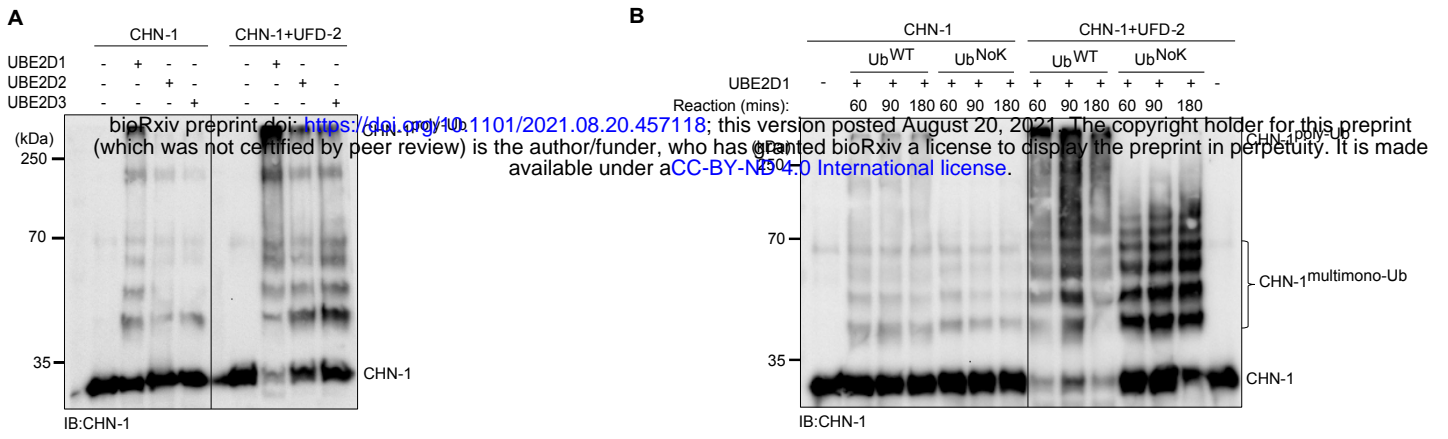
1089 Vrablik, T.L., Petyuk, V.A., Larson, E.M., Smith, R.D., and Watts, J.L. (2015). Lipidomic and  
1090 proteomic analysis of *Caenorhabditis elegans* lipid droplets and identification of ACS-4 as a lipid  
1091 droplet-associated protein. *Biochim. Biophys. Acta - Mol. Cell Biol. Lipids*.

1092 Waterhouse, A., Bertoni, M., Bienert, S., Studer, G., Tauriello, G., Gumienny, R., Heer, F.T., De  
1093 Beer, T.A.P., Rempfer, C., Bordoli, L., et al. (2018). SWISS-MODEL: Homology modelling of  
1094 protein structures and complexes. *Nucleic Acids Res.*

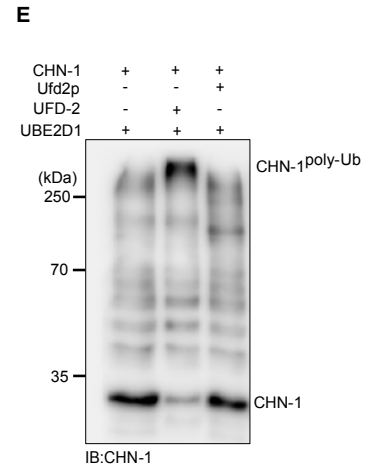
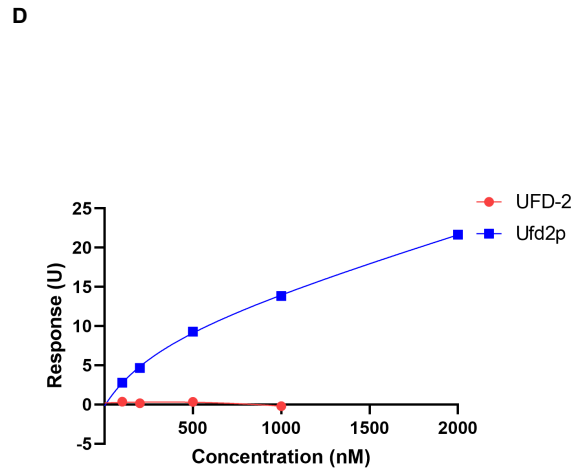
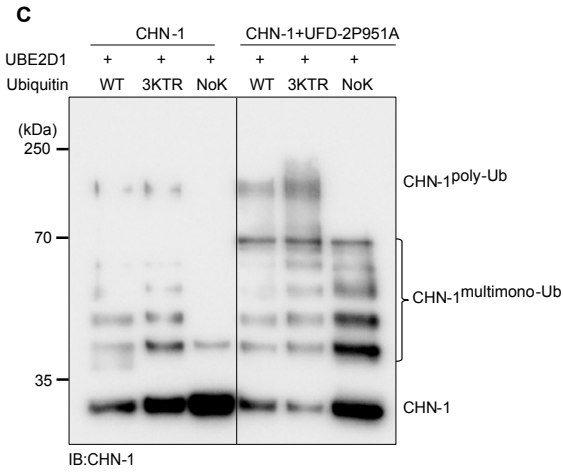
1095 Waterhouse, A.M., Procter, J.B., Martin, D.M.A., Clamp, M., and Barton, G.J. (2009). Jalview  
1096 Version 2-A multiple sequence alignment editor and analysis workbench. *Bioinformatics*.

1097 Wojcik, J., Boneca, I.G., and Legrain, P. (2002). Prediction, assessment and validation of protein  
1098 interaction maps in bacteria. *J. Mol. Biol.*

1099 Xu, Z., Devlin, K.I., Ford, M.G., Nix, J.C., Qin, J., and Misra, S. (2006). Structure and  
1100 Interactions of the helical and U-box domains of CHIP, the C terminus of HSP70 interacting  
1101 protein. *Biochemistry*.  
1102 Ye, Z., Needham, P.G., Estabrooks, S.K., Whitaker, S.K., Garcia, B.L., Misra, S., Brodsky, J.L.,  
1103 and Camacho, C.J. (2017). Symmetry breaking during homodimeric assembly activates an E3  
1104 ubiquitin ligase. *Sci. Rep.*  
1105 Zhang, H., Amick, J., Chakravarti, R., Santarriaga, S., Schlanger, S., McGlone, C., Dare, M.,  
1106 Nix, J.C., Scaglione, K.M., Stuehr, D.J., et al. (2015). A Bipartite Interaction between Hsp70 and  
1107 CHIP Regulates Ubiquitination of Chaperoned Client Proteins. *Structure*.  
1108 Zhang, H., Liu, Z., Ma, S., Zhang, H., Kong, F., He, Y., Yang, X., Wang, Y., Xu, H., Yang, A., et  
1109 al. (2016). Ratio of S-adenosylmethionine to S-adenosylhomocysteine as a sensitive indicator of  
1110 atherosclerosis. *Mol. Med. Rep.*  
1111 Zhang, M., Windheim, M., Roe, S.M., Pegg, M., Cohen, P., Prodromou, C., and Pearl, L.H.  
1112 (2005). Chaperoned ubiquitylation - Crystal structures of the CHIP U box E3 ubiquitin ligase and  
1113 a CHIP-Ubc13-Uev1a complex. *Mol. Cell*.  
1114  
1115



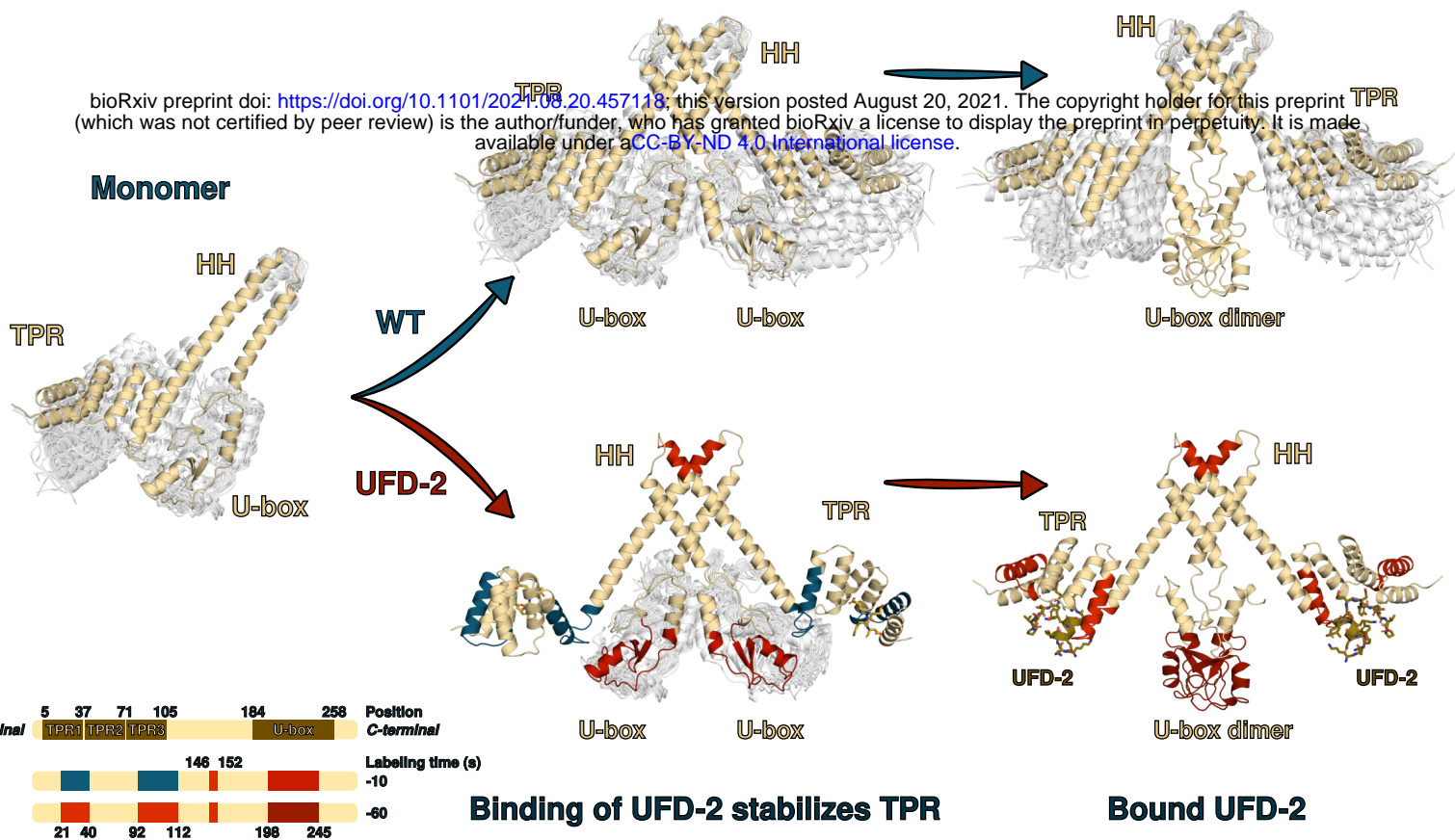
bioRxiv preprint doi: <https://doi.org/10.1101/2021.08.20.457118>; this version posted August 20, 2021. The copyright holder for this preprint (which was not certified by peer review) is the author/funder, who has granted bioRxiv a license to display the preprint in perpetuity. It is made available under a [CC-BY-NC 4.0 International license](#).



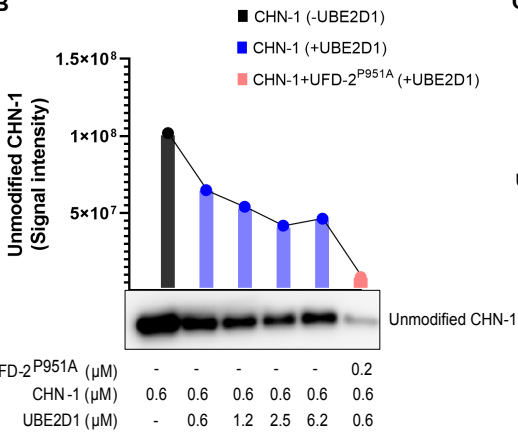


A

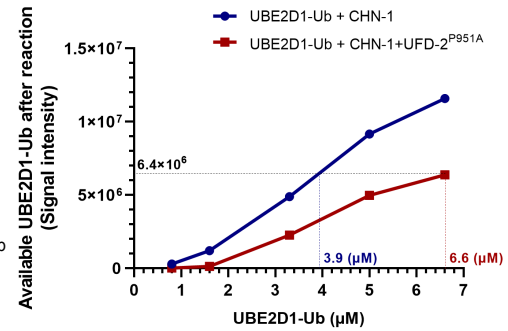
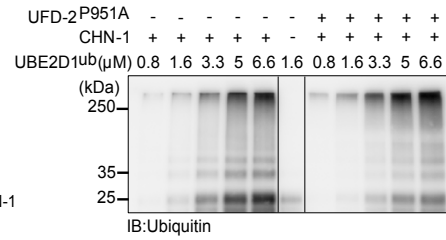
bioRxiv preprint doi: <https://doi.org/10.1101/2021.08.20.457118>; this version posted August 20, 2021. The copyright holder for this preprint (which was not certified by peer review) is the author/funder, who has granted bioRxiv a license to display the preprint in perpetuity. It is made available under a [CC-BY-ND 4.0 International license](https://creativecommons.org/licenses/by-nd/4.0/).

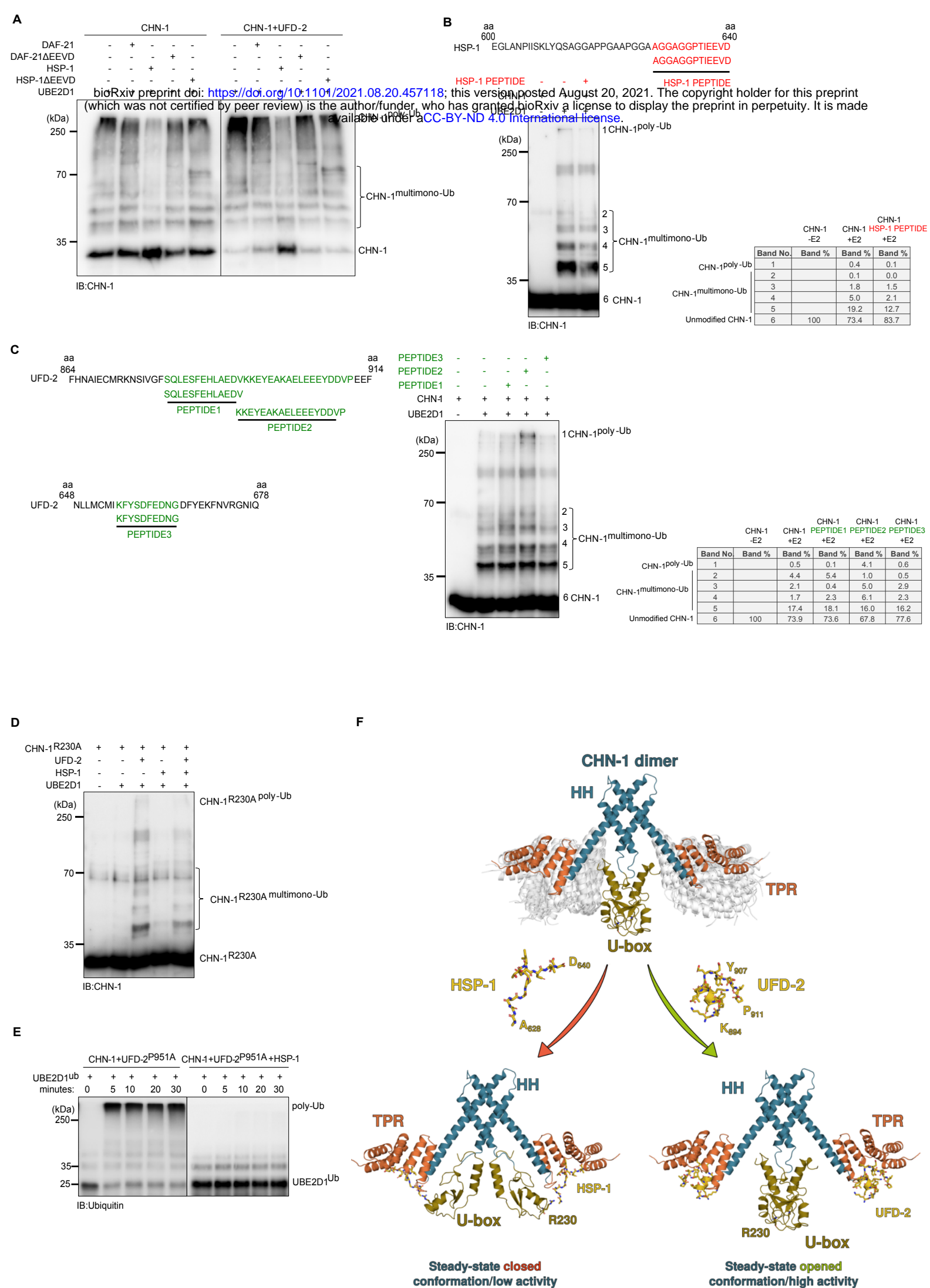


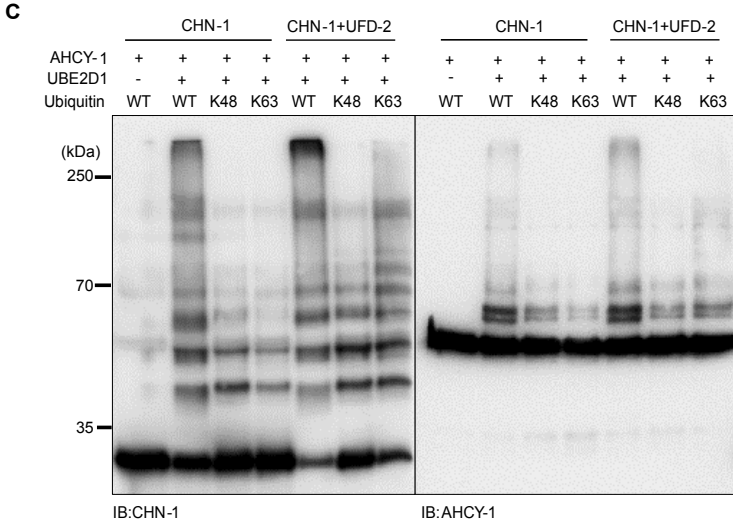
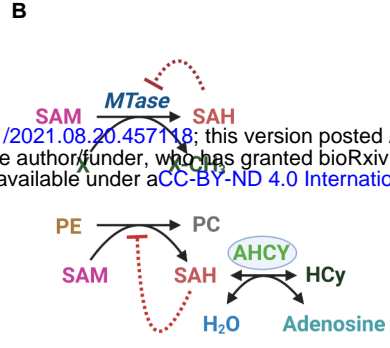
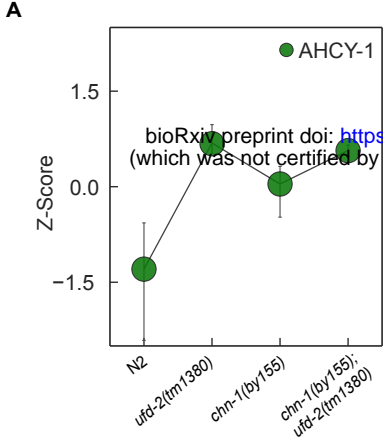
B



C







Band No.	AHCY-1		AHCY-1 UFD-2	
	CHN-1 -E2	CHN-1 +E2	CHN-1 -E2	CHN-1 +E2
1		0.1		4.3
2		0.5		0.5
3		2.0		2.0
4		7.7		7.1
5		3.0		4.3
6	100	86.7		81.7

